Effects of High Resolution and Spinup Time on Modeled North Atlantic Circulation

CHRISTOPHER DANEK

Alfred Wegener Institute for Polar and Marine Research, Bremerhaven, and MARUM–Center for Marine Environmental Sciences, University of Bremen, Bremen, Germany

PATRICK SCHOLZ

Alfred Wegener Institute for Polar and Marine Research, Bremerhaven, Germany

GERRIT LOHMANN

Alfred Wegener Institute for Polar and Marine Research, Bremerhaven, and MARUM–Center for Marine Environmental Sciences, University of Bremen, Bremen, Germany

(Manuscript received 3 July 2018, in final form 3 February 2019)

ABSTRACT

The influence of a high horizontal resolution (5–15 km) on the general circulation and hydrography in the North Atlantic is investigated using the Finite Element Sea Ice–Ocean Model (FESOM). We find a stronger shift of the upper-ocean circulation and water mass properties during the model spinup in the high-resolution model version compared to the low-resolution (~1°) control run. In quasi equilibrium, the high-resolution model is able to reduce typical low-resolution model biases. Especially, it exhibits a weaker salinification of the North Atlantic subpolar gyre and a reduced mixed layer depth in the Labrador Sea. However, during the spinup adjustment, we see that initially improved high-resolution features partially reduce over time: the strength of the Atlantic overturning and the path of the North Atlantic Current are not maintained, and hence hydrographic biases known from low-resolution ocean models return in the high-resolution quasi-equilibrium state. We identify long baroclinic Rossby waves as a potential cause for the strong upper-ocean adjustment of the high-resolution model and conclude that a high horizontal resolution improves the state of the modeled ocean but the model integration length should be chosen carefully.

1. Introduction

Numerical climate models operate on increasingly finer grid sizes as the performance of parallelized super computers increases. Whether a model can represent a geophysical process depends on the model formulation and discretization. Since the spatial scale of oceanic eddies is $O(1–100)$ km (first baroclinic Rossby radius of deformation; Chelton et al. 1998), the ocean model grid resolution needs to be on the same order to represent these ubiquitous small-scale features (Chelton et al. 2011). Alternatively, their effects must be parameterized. This is necessary as in state-of-the-art general circulation models (GCMs) the oceanic components run on horizontal resolutions of ~1° (e.g., Han et al. 2016).

Furthermore, a spinup is necessary to let the model adjust from initial conditions toward its own dynamics. While the geostrophic adjustment as well as boundary and Kelvin wave adjustments occur from after a few model days to years, long baroclinic Rossby wave basin-crossing travel times reach several decades at high latitudes (Cherniawsky and Mysak 1989; Chelton and Schlax 1996). Moreover, the deep ocean adjustment needs several thousand model years to reach a

Denotes content that is immediately available upon publication as open access.

Corresponding author: Christopher Danek, cdanek@awi.de

DOI: 10.1175/JPO-D-18-0141.1

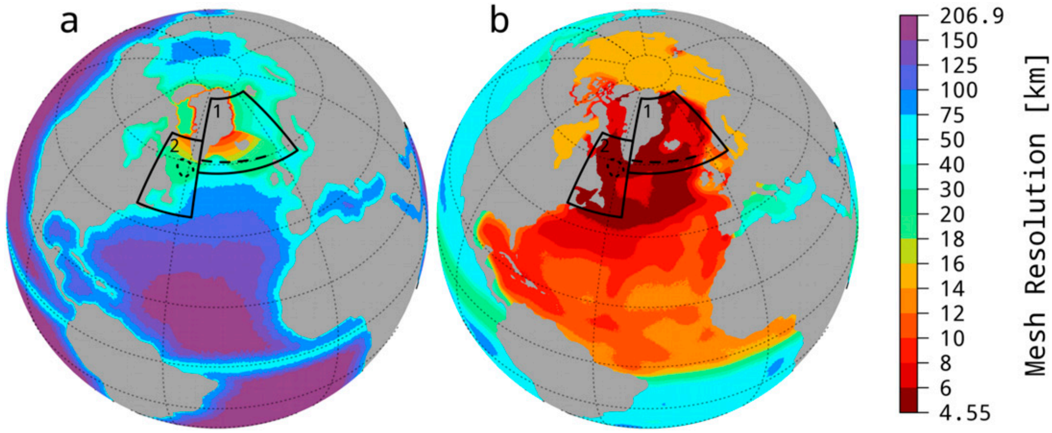

FIG. 1. Horizontal mesh resolution (km) of the (a) low- and (b) high-resolution models. The resolution is increased at the boundaries, the equator, in the subpolar gyre (both panels) and in areas of high SSH variability, steep bathymetry, and high horizontal temperature gradients as detected by observations [in (b) only, see methods]. The two boxes show Nordic Sea (labeled 1) and Labrador Sea (labeled 2) areas for sea ice extent time series, and the dashed lines mark the index area in the Labrador Sea and the ~60°N cross section in the eastern North Atlantic.

quasi-equilibrium state because of the slow diffusion of active tracers (Danabasoglu et al. 1996; McWilliams 1998). Due to the high computational costs, many high-resolution ocean modeling studies have much shorter simulation lengths of O(1–20) years (Treguier et al. 2005; Bryan et al. 2007; Rattan et al. 2010; Talandier et al. 2014; Marzocchi et al. 2015; Dupont et al. 2015; Hewitt et al. 2016; Iovino et al. 2016).

However, low-resolution model deficiencies such as a too weak overturning, incorrect current pathways, or hydrographic biases are partially corrected using a high horizontal model resolution (e.g., Hurlburt and Hogan 2000; Treguier et al. 2005; Bryan et al. 2007; Talandier et al. 2014; Marzocchi et al. 2015). On the other hand, incorrect circulation pathways, missing small-scale processes, or an insufficient vertical model resolution lead to model biases such as a too saline subpolar gyre (Treguier et al. 2005; Brandt et al. 2007; Chanut et al. 2008; Rattan et al. 2010; Xu et al. 2013; Marzocchi et al. 2015) as well as too deep mixed layer depths (MLDs) in the Labrador Sea (Oschlies 2002; Fox-Kemper et al. 2008; Danabasoglu et al. 2014, 2016; Heuzé 2017).

In this study, we evaluate the impact of a 5–15-km horizontal resolution on the modeled North Atlantic Ocean large-scale circulation and water mass structure. We use the global Finite Element Sea Ice–Ocean Model (FESOM; Danilov et al. 2004; Q. Wang et al. 2014) with the capability of a local mesh refinement. To achieve a quasi-equilibrium model state, we integrated the model for ~300 model years. The combination of a high spatial resolution and a long model integration time enables us to study systematically the effects of explicitly resolved features and the effect of spinup cycles on the large-scale circulation.

2. Model description

We used the global FESOM (Danilov et al. 2004; Q. Wang et al. 2014) in a locally eddy-resolving resolution in the North Atlantic (5–15 km, 61 vertical levels) and a ~1° low-resolution control run (from 10 to 200 km, 39 vertical levels; Fig. 1; see section 2a for mesh details). In contrast to many other climate models, FESOM is spatially discretized on irregular sized triangles at the surface. These 2D triangles are repeated in the vertical direction (z coordinate) so that the 3D nodes have their horizontal position aligned with the surface nodes. The resulting prisms are cut into three tetrahedral elements, on which the model performs. This spatial discretization allows for an adjustable mesh size in regions of interest and along irregular terrain (e.g., coastlines and ocean floor).

FESOM solves the Boussinesq hydrostatic primitive equations for the ocean via linear basis functions at all nodes (Galerkin formulation; Danilov et al. 2004; Wang et al. 2008). The smallest mesh element determines the model time step. The dynamic–thermodynamic sea ice model is described in (Timmermann et al. 2009).

For numerical stability in the presence of fast currents, an anisotropic (larger in direction of fast flow) biharmonic viscosity A_h reduces momentum with a background value $A_{h,0} = -3 \times 10^{13}\,\mathrm{m^4\,s^{-1}}$. To keep this nonphysical momentum friction as small as possible, A_h is scaled that it 1) decreases with grid size to the third power ($A_h = A_{h,0}$ at 100-km grid size), 2) doubles in a $\pm 10°$ latitude band around the equator, and 3) increases in regions of large horizontal shear [Smagorinsky (1963); see Wang et al. (2008) for implementation in FESOM's linear basis functions].

Physical parameterizations are implemented for tracer mixing along isopycnals (Redi diffusion; Redi 1982) and tracer advection due to adiabatic stirring (GM, an additional velocity is added to the tracer equation; Gent and McWilliams 1990). Both are formulated together as the Griffies skew flux (Griffies et al. 1998) with a background horizontal diffusion $K_{h,0} = 1500\,\mathrm{m^2\,s^{-1}}$. The strength of this subgrid-scale (SGS) flux is scaled with the stratification of the flow and the horizontal grid resolution. The scaling with the horizontal resolution is limited by $2\,\mathrm{m^2\,s^{-1}}$ at the lower end and the background horizontal diffusion $K_{h,0}$ above 50-km local horizontal resolution (see Fig. A1 in the appendix). At grid resolutions of $O(1\text{–}10)$ km the flux is very small but not disabled (for details see Q. Wang et al. 2014).

Diapycnal (vertical) mixing is implemented via the k-profile parameterization (KPP; Large et al. 1994) with a background vertical diffusivity $K_{v,0}$ for tracers increasing from $10^{-5}\,\mathrm{m^2\,s^{-1}}$ at the sea surface to $10^{-4}\,\mathrm{m^2\,s^{-1}}$ at the ocean floor (see Fig. 11 in Q. Wang et al. 2014) and a background vertical viscosity $A_{v,0} = 10^{-4}\,\mathrm{m^2\,s^{-1}}$ for momentum. In cases of static instability (high-density above low-density water) both coefficients equal $1\,\mathrm{m^2\,s^{-1}}$ to ensure a rapid mixing (convective adjustment). Mixing due to double diffusion is disabled as well as tides. For numerical stability, a sea surface salinity (SSS) restoring (or relaxation) toward climatology with a typical piston velocity $v_p = 50\,\mathrm{m}\,(300\ \mathrm{days})^{-1} \approx 1.93 \times 10^{-6}\,\mathrm{m\,s^{-1}}$ is applied. If this restoring is disabled, the SSS becomes unrealistically high at single nodes around Greenland (not shown), possibly due to missing sea ice–ocean interactions as noted in Marsh et al. (2010) (the restoring is largest in the presence of sea ice).

FESOM was successfully used for modeling the general oceanic circulation, variability of the North Atlantic Deep Water formation rates and sea ice distribution (Sidorenko et al. 2011; Scholz et al. 2013, 2014) as well as chlorophyll distributions (biogeochemical coupling; Schourup-Kristensen et al. 2014). FESOM's local mesh refinement allows for a realistic modeling of water mass properties in domains with high complexity including small spatial scales, for example, Fram Strait (Ionita et al. 2016), the Canadian Arctic Archipelago (Wekerle et al. 2013), Greenland (Wang et al. 2012), or the Ross Sea (Wang et al. 2010).

a. *Local mesh refinement*

In this study we use two different mesh configurations with locally refined resolutions (low and high resolution; Fig. 1). Both model grids have an increased resolution along the coastline and at the equator to ensure that oceanic currents along the coastline as well as coastal and equatorial upwelling processes can be adequately simulated. Furthermore, the low-resolution model mesh (Fig. 1a) has an increased resolution in the northern hemispheric deep water formation areas and is described in Scholz et al. (2013, 2014).

The high-resolution model configuration (Fig. 1b) features additionally increased resolution in the subpolar North Atlantic and in areas with 1) enhanced sea surface height (SSH) variability as measured by satellite altimeter data (AVISO), 2) steep bathymetric slopes based on ETOPO1 (Amante and Eakins 2009), and 3) high horizontal temperature gradients in 200-m depth (Locarnini et al. 2013).

This high-resolution mesh exhibits horizontal resolutions of ~10 km along the North Atlantic coastline (~5 km along Greenland and Labrador), an increased resolution along the equator (from ~45 km at 10°S to ~14 km at 20°N) and a varying resolution of ~8–15 km in the subtropical gyre. The average resolution of the subpolar gyre is ~5 km up to the Fram Strait. The Arctic Ocean is resolved by ~15-km grid size. With this mesh configuration which has a resolution in the Atlantic that is close to the deformation radius of eddies we ensured that the model is able to resolve important oceanic currents along the coast line as well as energetic fronts. In both models the vertical resolution is finer in the upper 200 m to better resolve the boundary layer and becomes coarser with depth. The high-resolution model exhibits 61 vertical levels and therefore resolves the first baroclinic mode of the ocean (Stewart et al. 2017). In contrast, the low-resolution control model is discretized on 39 vertical levels, not capturing this mode. The depth intervals range from 10 to 300 m in the low-resolution model and from 10 to 150 m in the high-resolution model.

b. *Spinup strategy*

The models were forced by the 6-hourly atmospheric reanalysis dataset CORE-II (Large and Yeager 2009) covering the period 1948–2009 and were initialized with the Polar Science Center Hydrographic Climatology (PHC3; Steele et al. 2001). Turbulent fluxes between the ocean/ice and the atmosphere were calculated using the bulk formulae from Large and Yeager (2004).

Previous FESOM studies of Sidorenko et al. (2011), Wang et al. (2012), and Scholz et al. (2013) have shown that a spinup time of 250–300 years is necessary to bring the upper and intermediate ocean into a quasi-equilibrium state. For that reason we performed five consecutive

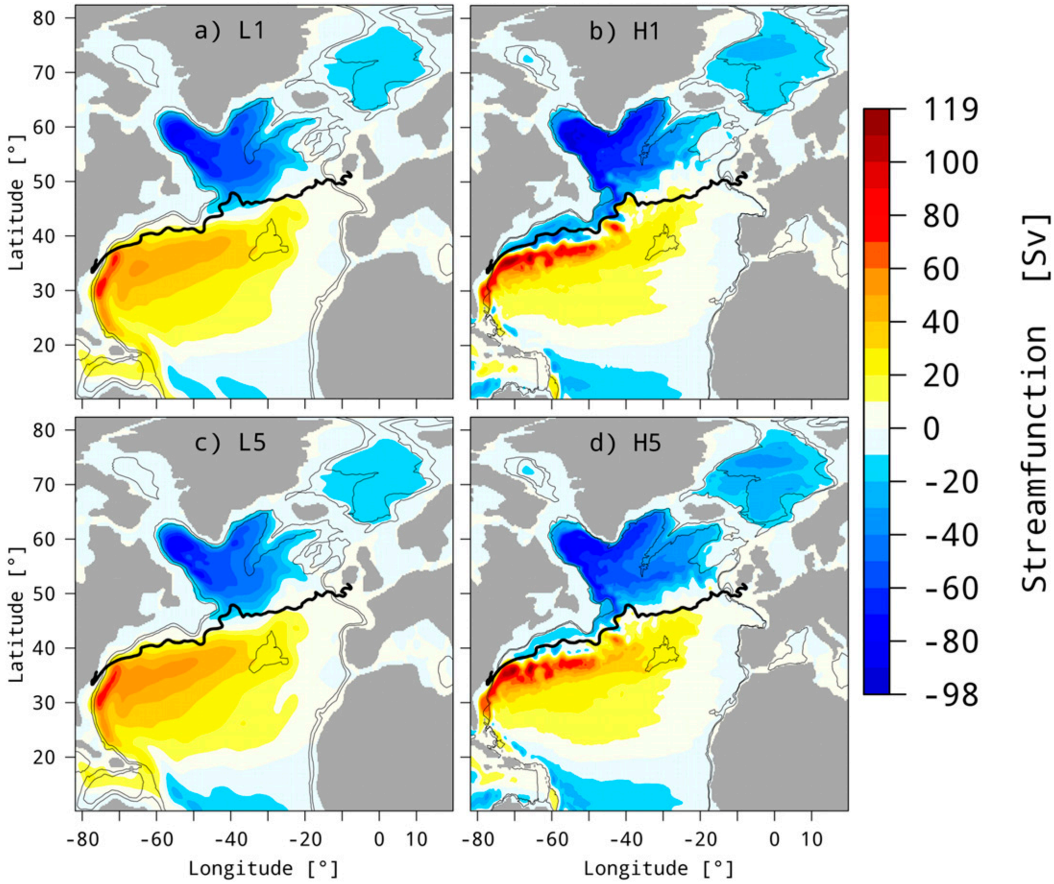

FIG. 2. Average (1961–2009) horizontal barotropic streamfunction (colors; Sv; 1 Sv = $10^6\,m^3\,s^{-1}$; positive clockwise; 10-Sv contour interval) of (a),(b) first and (c),(d) fifth spinups of (left) low- and (right) high-resolution models. The thick black line shows the average (1993–2009) zero SSH as derived by satellite altimetry (AVISO). Thin black lines are 1- and 2-km isobaths.

spinup cycles each with a length of 62 years in order to reach a quasi-equilibrium model state (310 years in total, monthly model output was saved). For each spinup cycle the last output of the preceding spinup was used as a new initialization as it is suggested in the CORE and CORE-II protocols (Griffies et al. 2012; Danabasoglu et al. 2014) and applied in other ocean modeling studies (Lohmann et al. 2009; Karspeck et al. 2017; He et al. 2016).

Hereafter, the performed model experiments are named L1, L2, . . . , L5 and H1, H2, . . . , H5 for the combination of the two model resolutions (low and high; Figs. 1a,b) and the number of the spinup cycle (1–5). If time average periods are not given explicitly, the whole spinup period 1948–2009 (62 years) is used.

3. Results

a. North Atlantic circulation

The average (1961–2009) modeled horizontal North Atlantic barotropic circulation is composed of a clockwise rotating subtropical and anticlockwise rotating subpolar gyre, separated by the Gulf Stream and its extension the North Atlantic Current (NAC; Fig. 2; Sverdrups, 1 Sv = $10^6\,m^3\,s^{-1}$). The high-resolution model exhibits a stronger subpolar and subtropical gyre transport, as well as enhanced small-scale features when compared to the low-resolution control run. After the first spinup cycle (L1 and H1, Figs. 2a,b) the high-resolution Gulf Stream separates from the North American coast several degrees further south, is of narrower shape and exhibits transports around 100 Sv (peak values around 120 Sv), around twice the transports of the low-resolution Gulf Stream. North of the Gulf Stream (south of Newfoundland) an anticlockwise recirculation cell of 30–40 Sv is present in the H1 run but almost absent in the L1 run. Further downstream, the high-resolution model shows a distinct transition behavior between the Gulf Stream and its extension the North Atlantic Current comprising a Northwest Corner–like circulation pattern. The average (1993–2009) position of zero SSH as derived by satellite altimetry (AVISO) in

Fig. 2 (thick black line) indicates the observed boundary between the subtropical and subpolar gyres. The subpolar gyre is also intensified in the high-resolution model with enhanced transports in the Labrador, Irminger, Iceland, and Nordic Seas.

The gyre structures change from the first to the fifth spinup cycles (i.e., after ~300 model years; Figs. 2c,d) in the high-resolution model, whereas they remain rather unchanged in the low-resolution control run. The anticlockwise recirculation cell north of the Gulf Stream axis decreased by ~50% to 15 Sv. The transition area between the Gulf Stream and North Atlantic Current including the Northwest Corner exhibits reduced transports with increasing number of spinup cycles. Although the general shape and strength of the Gulf Stream west of ~50°W persists through the spinup cycles, the current penetrates further east in H5 compared to H1 (Figs. 2b,d)—the Gulf Stream becomes more zonal with spinup time. The high-resolution North Atlantic Current shows a similar behavior: the anticlockwise transports in the Iceland basin (south of Iceland) increased around 20 Sv meaning that the North Atlantic Current shifted from its northeast direction in the first spinup to a more eastward directed flow in the fifth spinup. Similarly, the cyclonic circulation in the Greenland–Iceland–Norwegian (GIN) Seas increases by ~10 Sv. In contrast, the cyclonic circulations in the Labrador and Irminger Sea decrease with spinup time by 10–15 Sv. The low-resolution model does not show these changes of the horizontal barotropic streamfunction with spinup time.

Figure 3 shows depth anomalies of the 17°C isotherm across the North Atlantic basin at 30°N of the fifth spinups of both models as a function of longitude and time (m; seasonal mean 1948–2009 removed; positive values indicate deeper depths). On average, this isotherm is located at approximately 250-m depth in both models. Depth anomaly contours of several tens of meters travel westward in the high-resolution model throughout the forcing period with a velocity of $3.12 \pm 0.07\,\mathrm{cm\,s^{-1}}$ as inferred by Radon transform [straight line starting from the lower right in Fig. 3b; see chapter 6.4 of Robinson (2010) and references therein for a description of the Radon transform; the velocity uncertainty was derived via Eq. (A3) of Alvera-Azcárate et al. (2009), dotted line in Fig. 3b]. In the low-resolution model, in contrast, vertical isotherm displacements west of the Mid-Atlantic Ridge (MAR) are rather stationary in space (Fig. 3a; the model bathymetry in km is added as black line with corresponding axis on the lower right of Fig. 3b). The isotherm depth anomalies were filtered with a Gaussian Nadaraya–Watson filter (Fan and Gijbels 1996) with a bandwidth of 3° in longitude direction to reduce small-scale noise as used similarly in, for example, Abe et al. (2016). Furthermore, note that similar westward wave propagations of several cm magnitude can be detected in the SSH anomalies (not shown) as well as in the first m baroclinic WKB approximated horizontal velocity modes $R_m \overset{\mathrm{WKB}}{\approx} c_{g,m}\, N\, S_{0,m}\, g^{-1} \cos\left[c_{g,m}^{-1} \int_{-H}^{z} N(z)\, dz\right]$, where $c_{g,m} \overset{\mathrm{WKB}}{\approx} (m\pi)^{-1} \int_{-H}^{0} N(z)\, dz$ represents the mth baroclinic gravity wave speed with buoyancy frequency $N = (-g\rho^{-1}\, \partial_z \rho)^{1/2}$, acceleration due to gravity g and in situ density ρ. Parameter $S_{m,0} = (c_{g,m} N^{-1})^{1/2}$ serves as a dimensionless normalization constant [see Eq. (3.72) in Vallis 2017, p. 117]. These modes represent wave solutions to the horizontal part of the linearized quasigeostrophic potential vorticity equation of a flat bottom ocean with zero background flow and associated vertical wavenumber m [Eq. (3.56) in Vallis 2017, p. 115]. Further information can be found in section 6.11 of Gill (1982). Shown in the appendix (see Fig. A4), similar to Fig. 3, is exemplary R_1 and R_2 in 500-m depth as a function of longitude and time. Spatiotemporal anomalies (seasonal mean 1948–2009 removed) are much larger in the high- compared to the low-resolution model, travel westward with a similar propagation velocity as the isotherm depth anomalies ($3.4 \pm 0.02\,\mathrm{cm\,s^{-1}}$) and are enhanced west of the MAR. With increasing wavenumber m, the differences between the two models diminish (not shown). Notice that the average vertical structure of R_m, showing a surface intensification and m zero crossings of each mth mode, does not differ much between the models (as shown in Fig. A3).

The average (1961–2009) Atlantic meridional overturning circulation (AMOC; Sv; Fig. 4) shows generally increased maximum transports in the high- compared to the low-resolution model. In particular, the maximum of the upper clockwise circulation cell in H1 (~23 Sv) approximately doubles compared to L1 (~13 Sv). An anticlockwise circulation cell in the deep ocean is almost absent in both models in the first model spinup. After five spinup cycles the upper clockwise circulation maxima decreased to 11 Sv in L5 (15% reduction), and 16 Sv in H5 (30% reduction). In contrast, the strength of the lower anticlockwise circulation cell increased from −1 to −3 Sv in both models and is stronger in the low-resolution model. This change is also reflected in a shallower interface between both circulation cells from 3.8 (L1) to 3 km (L5) and from 3.8 (H1) to 3.4 km (H5) in the tropics and subtropics.

The decadal evolution of the overturning maxima at different latitudes shows a similar variability in time, independent of model resolution and number of spinup cycles (Fig. 5). Generally, the overturning maxima are increased by ~50% (15%) in the high- compared to the low-resolution model at 26.5°N (41°N). From the first to

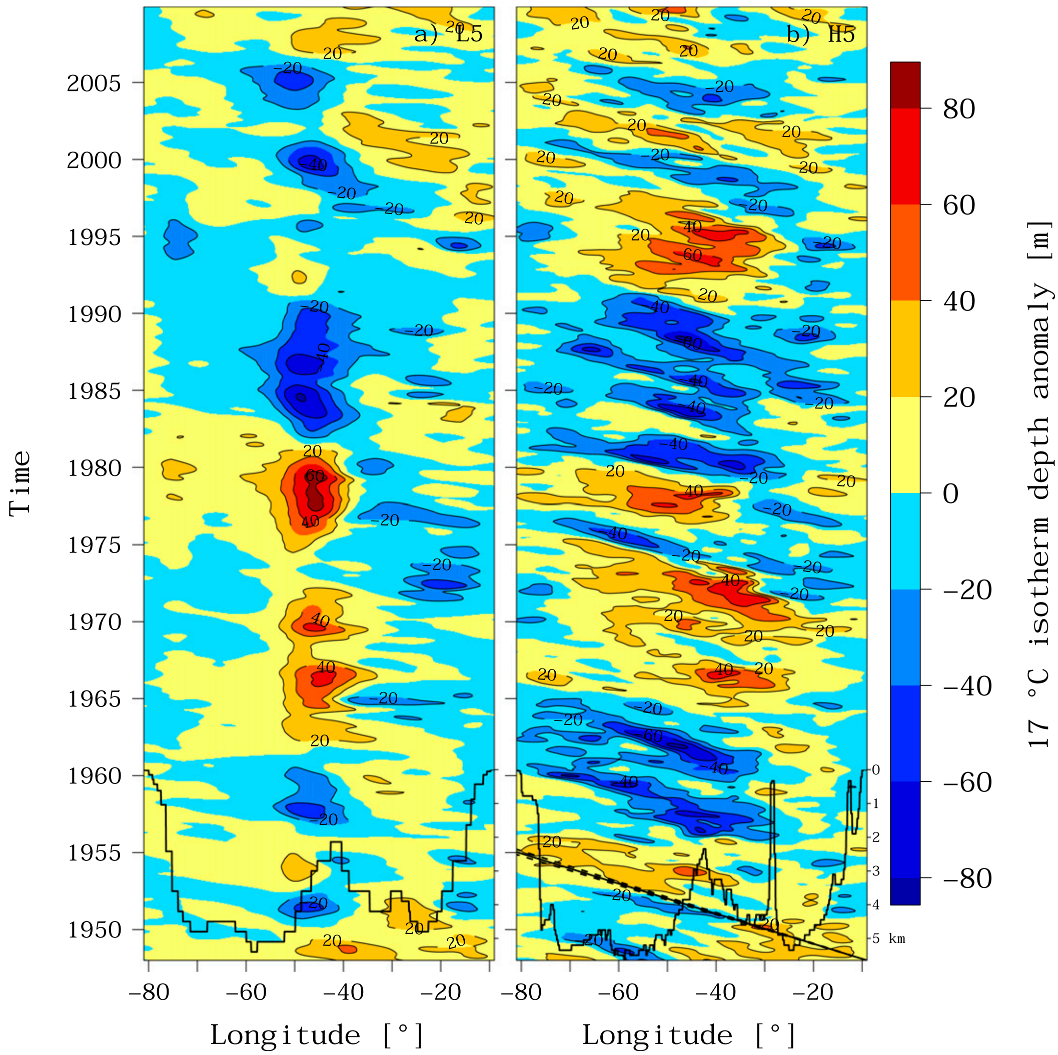

FIG. 3. The 17°C isotherm depth anomalies of the fifth spinups of (a) low- and (b) high-resolution models as a function of longitude and time along 30°N in the Atlantic (colors; m; seasonal mean 1948–2009 removed; positive values indicate deeper depths). The anomalies were smoothed with a Gaussian Nadaraya–Watson filter with a bandwidth of 3° in longitude direction. The model bathymetry is added as black line [km; axis on the lower right of (b)]. The straight black and dotted lines in (b) show a westward velocity of $3.12 \pm 0.07\ \mathrm{cm\,s^{-1}}$ as determined by Radon transform (see text for details). The average (1948–2009) depth of the 17°C isotherm is around 250 m in both models.

the fifth spinup cycles the average (1948–2009) overturning decreases around 20% in both models and at both latitudes toward quasi equilibrium. The low-resolution overturning reduces by 14% (12%), 10% (8.5%), and 2.5% (1.8%) from the first to second to third to fourth spinup cycle at 26.5°N (41°N). Similar values are obtained for the high-resolution model with 12% (15%), 6.6% (6.7%), and 1.6% (0.5%) at 26.5°N (41°N). In both models this spinup adjustment "converges" after four spinup cycles (248 model years) in the sense that the change from the fourth to the fifth cycle changes sign and is of similar magnitude as the change from the third to the fourth: 0.8% (1.2%) and 0.7% (0.4%) increase in the low- and high-resolution models respectively at 26.5°N (41°N).

At 26.5°N, the overturning of the H1 run shows an overlap from the years 2004–09 with observations of the RAPID array (Smeed et al. 2017; green line in Fig. 5a) as well as an SSH-based estimate of Frajka–Williams (2015) (black line in Fig. 5a). However, the spinup adjustment leads to transports weaker than observed at that latitude. At 41°N the situation is different: here, the high-resolution maximum overturning rates exceed these measured by Willis (2010) even after the

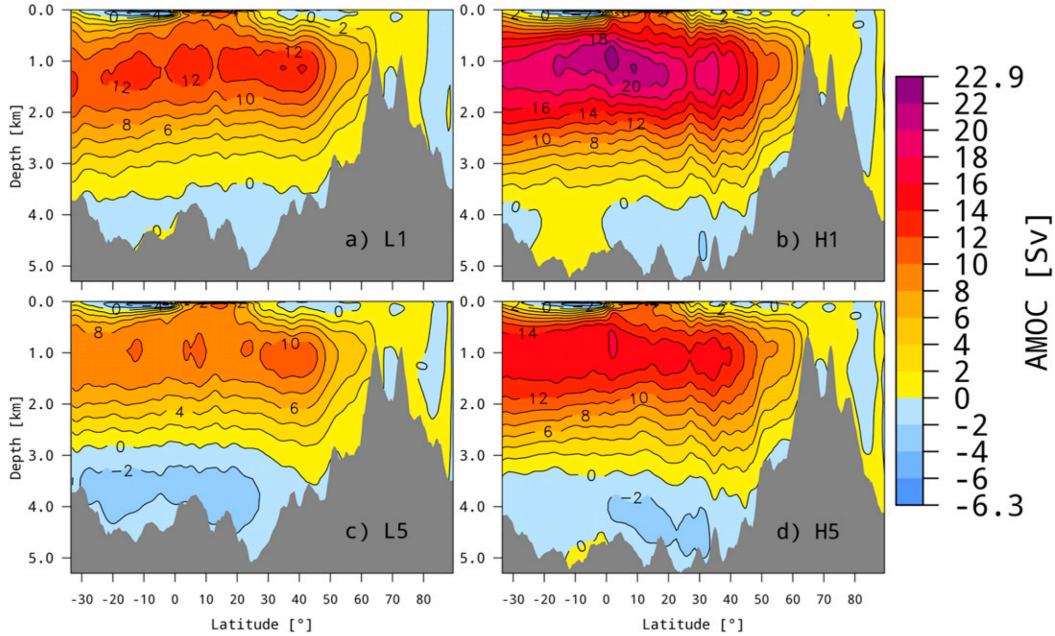

FIG. 4. Average (1961–2009) AMOC (Sv; positive clockwise; 2-Sv contour interval) of (a),(b) first and (c),(d) fifth (left) low- and (right) high-resolution models. A local smoothing window was applied for plotting.

spinup adjustment (within the observed upper uncertainty bounds). Initially, the L1 run exhibits the best agreement with the observations (green line in Fig. 5b). The L5 run, however, underestimates the overturning within the observed lower uncertainty bounds.

The total meridional North Atlantic Ocean heat transport $\mathrm{OHT} = \rho_{\mathrm{ref}}\, c_p \int_{\mathrm{West}}^{\mathrm{East}} \int_{\mathrm{Bottom}}^{\mathrm{Surface}} \overline{\upsilon\theta}\, dz\, dx$ (PW; 1 PW $= 10^{15}$ W), positive northward, where the overbar denotes the temporal mean, with meridional velocity υ (m s^{-1}), potential temperature θ (°C), constant reference density $\rho_{\mathrm{ref}} = 1027\,\mathrm{kg\,m^{-3}}$, and the specific heat capacity of seawater $c_p = 3985\,\mathrm{m^2\,s^{-2}\,K^{-1}}$, is shown in Fig. 6 (the product $\upsilon\theta$ was calculated at every model time step). The high-resolution OHT increases by 50%–70% compared to the low-resolution model with largest transports up to 1.2 PW in the subtropics in the H1 run. The spinup adjustment leads to an average OHT reduction of ~0.2 PW in both models. H1 covers the observed OHT range at 26.5°N from Johns et al. (2011), a total heat flux $\overline{\upsilon\theta}$ estimate taking spatial covariabilities of υ and θ into account (diamond in Fig. 6), while all other heat transports are too weak. At 47°N, in contrast, H1 overestimates the OHT and H3 and H5 show the best agreement with an inverse estimate from Ganachaud and Wunsch (2003), which is a mean heat flux $\overline{\upsilon}\,\overline{\theta}$ where correlated temporal variations are neglected (triangles in Fig. 6). At 30°S, all high-resolution model runs overestimate the Ganachaud and Wunsch (2003) solution while the low-resolution model runs are in the observed OHT range. North of 55°N until the pole the differences between the spinup runs of the respective models diminish.

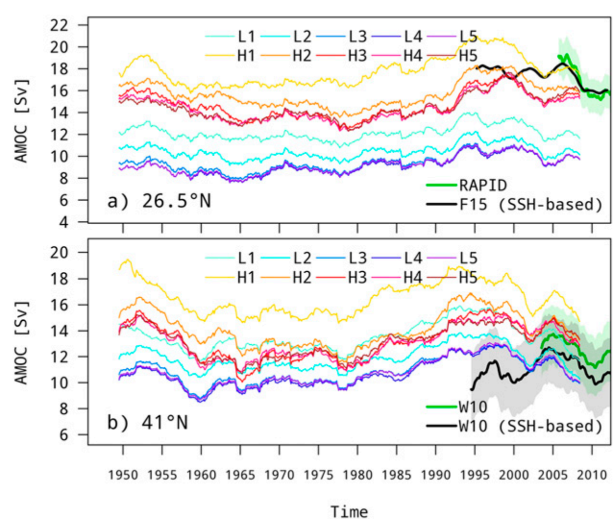

FIG. 5. Decadal evolution of AMOC maximum at (a) 26.5°N and (b) 41°N of all 5 spinups of low- and high-resolution models. In (a), thick green and black lines show overturning rates as observed (RAPID; Smeed et al. 2017; shading shows uncertainty given by authors) and an updated version of the SSH-based estimate of Frajka–Williams (2015), respectively In (b), they are an updated version of measured and SSH-based overturning rates from Willis (2010) (shading shows one standard deviation). All time series are low-pass filtered by a 3-yr running mean.

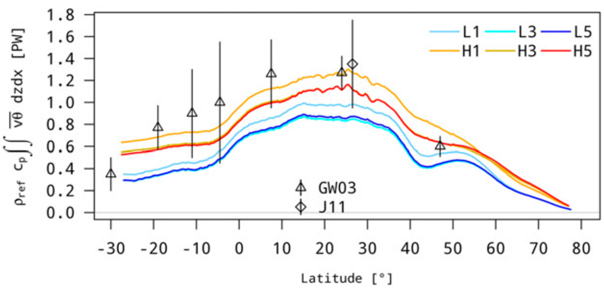

FIG. 6. Average (1961–2009) total North Atlantic meridional heat transport (PW; 1 PW = 10^{15} W; positive northward) of low- and high-resolution spinup runs (colored lines). GW03 (triangles) shows the inverse estimate of Ganachaud and Wunsch (2003) (uncertainties given by authors) and J11 (diamond) the observation at 26.5°N (MOCHA; Johns et al. 2011; uncertainty is one standard deviation). In the models, the product $\upsilon\theta$ is calculated at every time step.

The observed average (1993–2009) geostrophic surface velocity as derived by satellite altimetry (AVISO; Fig. 7a) shows a vigorous extension of the Gulf Stream in the form of fast (>25 cm s^{-1}) and narrow meanders. From the Northwest Corner around 51°N, 44°W the North Atlantic Current flows eastward and further downstream northeastward in the Iceland basin (with ~15 cm s^{-1}). H1 shows a Gulf Stream extension with features similar in strength, shape, and position as observed (Fig. 7b, full and not geostrophic modeled velocities are used since the results apply to both, not shown). The Northwest Corner, however, is half as strong as observed and the North Atlantic Current corresponds with the measured position but is stronger than observed (up to ~25 cm s^{-1}). Similarly, the Western Boundary Current (WBC) exhibits larger velocities along the coasts of Greenland and Newfoundland. After 5 spinup cycles the modeled high-resolution Northwest Corner is hardly visible and the whole Gulf Stream extension structure is shifted to the southeast with large (>15 cm s^{-1}) northeastward directed velocities east of 40°W (Fig. 7d). The low-resolution model, in contrast, exhibits neither narrow and fast meanders as Gulf Stream extension nor a Northwest Corner–like structure (Fig. 7c; here, only the fifth spinup is shown since the differences to the first spinup are negligible). The Gulf Stream extension is broad, slow and almost entirely eastward directed. From 40°W the current continues eastward more than twice as fast as measured (similar as in H5). At around 33°W the broad and slow current in L5 turns northeastward into the North Atlantic Current.

b. North Atlantic hydrography

The average (1965–2004) upper-ocean (0–100 m) temperature difference to the *World Ocean Atlas 2013* (*WOA13*; Locarnini et al. 2013) shown in Fig. 8 (°C; model minus *WOA13*) features warm as well as cold biases in the modeled North Atlantic. L1 exhibits a large (from >5° up to 8°C) warm bias north of the Gulf Stream axis and a large (from <−5° up to −9.5°C) cold bias at the Gulf Stream extension around 40°W (Fig. 8a). The Irminger Sea and the area of the Labrador Sea boundary current is ~2°C warmer than observed. The Nordic Seas (between Greenland and Norway) show a dipole of too cold (−4°C at 70°N) and too warm (2°C at 75°N) anomalies. In H1, the mentioned large biases at the Gulf Stream and its extension are not visible (Fig. 8b). In contrast, the vicinity of the North Atlantic Current (around 30°W and 55°N) is 2°–3°C warmer than observed as well as the East and West Greenland Current and Labrador Current. A similar cold bias as in L1 exists in the Greenland Sea that is surrounded by a too warm boundary current (3°C) along the coastline of Norway, Spitzbergen, and Greenland.

The temperature anomaly structure of the low-resolution model does not change with additional spinup cycles (Figs. 8c,e). Only the warm bias of the subpolar gyre reduces by ~1°C from L1 to L5. The solution of the high-resolution model, in contrast, shows several changes during the spinup procedure. The North Atlantic Current warm bias in H1 vanishes in favor of a large (<−5°C) cold bias in the Gulf Stream extension around 40°W from the first to the third model spinup comparable with the one of the low-resolution control runs (Figs. 8a,c). This behavior continues with spinup time and reaches very cold temperature anomalies up to −9°C similar as the low-resolution model (Fig. 8e). The warmer than observed temperature anomalies in the northern Nordic Seas also increase with spinup time by up to a 4°C. As in the low-resolution model, the Irminger and Labrador Sea become colder with spinup time and exhibit larger cold anomalies in the high-resolution model (from −2° to −3°C). Large-scale salinity anomalies (observations from Zweng et al. 2013) show similar model resolution and spinup length dependencies as described for temperature (Fig. A5).

Figure 9 shows the average summer (June–July, 2002–08) potential density σ_θ distribution of the northward and southward flowing water masses across ~60°N in the North Atlantic (integrated in 0.01 kg m^{-3} potential density bins, northward positive). All models transport light water masses northward above a southward directed high-density water flow. The low-resolution (L1, L5) northward flow peaks around σ_θ = 27.50 kg m^{-3}, with the peak in L1 slightly shifted toward denser water masses in the fifth spinup cycle. In contrast, the H1 northward transport has a maximum at σ_θ = 27.425 kg m^{-3} and exhibits a transition toward a broad range of lighter

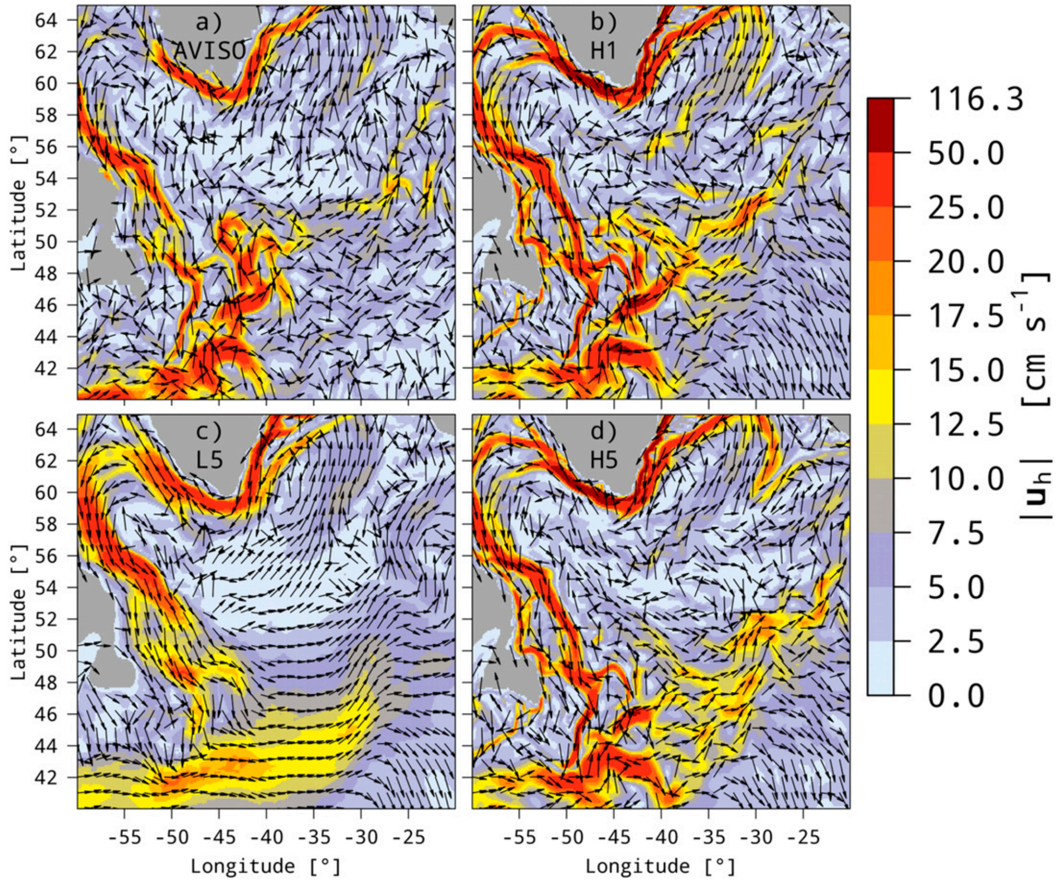

FIG. 7. Average (1993–2009) horizontal surface velocity norm (cm s^{-1}; irregular levels) and direction (arrows of constant length, not all plotted). (a) Geostrophic velocities as derived by satellite altimetry (AVISO), (b) the first spinup of the high-resolution model and (c),(d) the fifth spinups of low- and high-resolution models, respectively (differences between first and fifth low-resolution spinups are negligible). For the models the full (not geostrophic) velocities are shown.

water masses due to colder and fresher conditions from H1 to H5. L1, L5, and H1 resemble the observed northward flow (Sarafanov et al. 2012; black crosses) in magnitude but are shifted toward denser water masses compared to the observations. H5 is generally lighter and distributed over a broader density range (smaller amplitude) than observed. All modeled dense southward flows exhibit noticeable peaks and become lighter with spinup time. H5 matches the observed maximum southward transport at $\sigma_\theta = 28.85\,\mathrm{kg\,m^{-3}}$, while H1 being denser and L1 and L5 both being lighter. No clear pattern exists in the intermediate waters ($27.55 \le \sigma_\theta \le 27.80\,\mathrm{kg\,m^{-3}}$). The average (June–July, 2002–08) observed net transport across ~60°N has no distinct direction (0.1 ± 3 Sv, the rather large uncertainties are due to combination of different datasets; Sarafanov et al. 2012). All model solutions lie within these error bars. However, the H1 and H5 runs tend to show similar small net southward transports of −0.9 ± 0.9 Sv and −0.1 ± 0.6 Sv as the observations in contrast to the generally stronger L1 and L5 northward transports of +1.2 ± 0.5 Sv and +1.3 ± 0.4 Sv, respectively. Here, the model uncertainty is given by one standard deviation of the same 14-month period as the observations. Note that these density distributions (Fig. 9) do not change the general results if the long-term average (January–December, 1961–2009) is used (not shown).

Figure 10 shows the southward directed deep Denmark Strait overflow ($\upsilon < 0\,\mathrm{m\,s^{-1}}, \sigma_\theta > 27.8\,\mathrm{kg\,m^{-3}}$) through a section from Iceland to ~29°W (solid lines) as well as through a section from Iceland to Greenland (dashed lines). The observed Denmark Strait overflow from Jochumsen et al. (2017) through a section from Iceland to 29°W is shown as reference (black and gray lines). The overflow transport through the section from Iceland to 29°W of L1 (light blue solid line) features a mean value of ~−2 Sv, while the corresponding transport in H1 shows an enhancement by ~75% to a mean

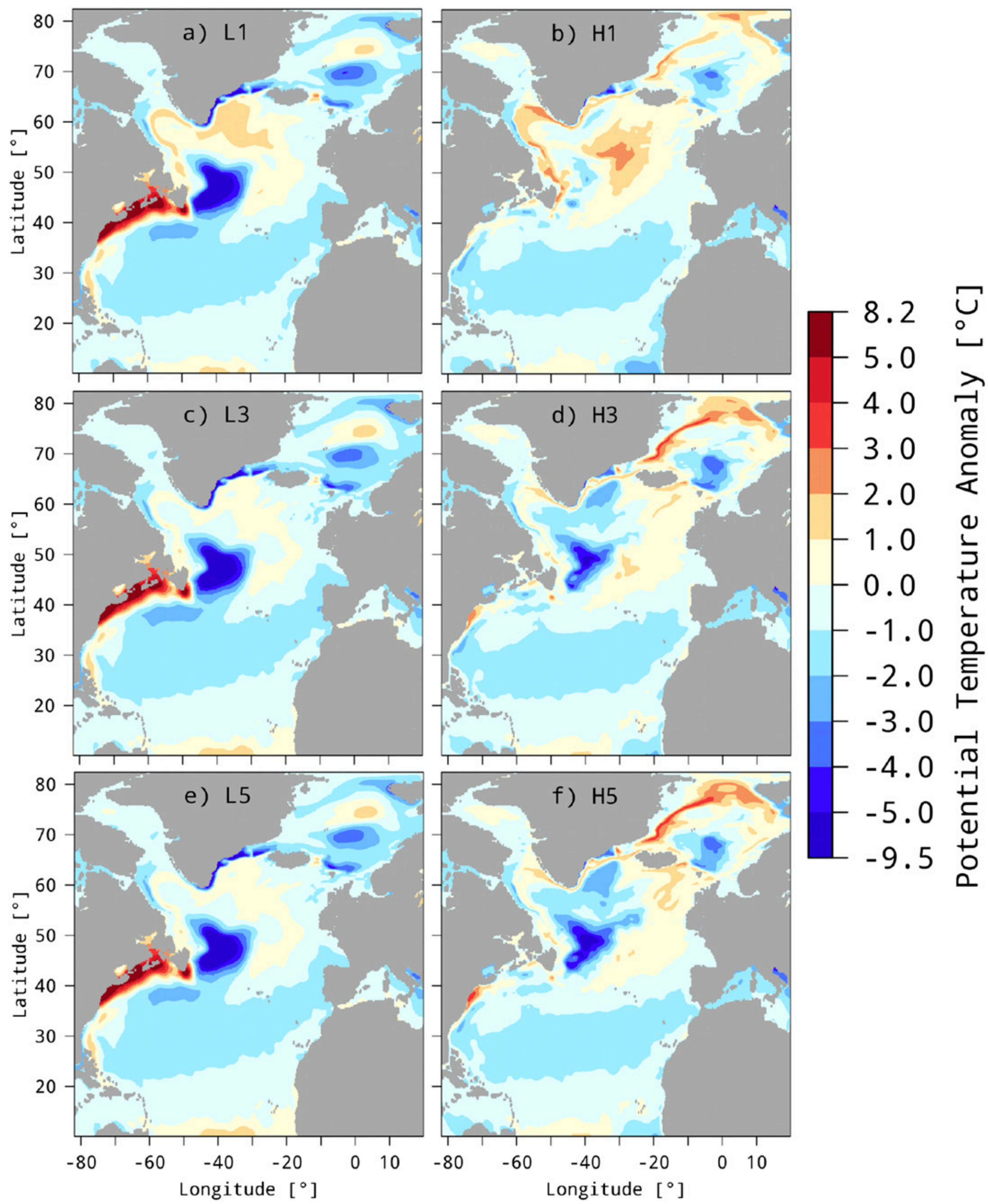

FIG. 8. Average (1965–2004, 0–100 m) potential temperature anomalies (model minus observation; °C) of (left) low- and (right) high-resolution models. Observations are from *WOA13* (Locarnini et al. 2013). Anomalies of (a),(b) first, (c),(d) third, and (e),(f) fifth model spinup minus observations.

value of ~ -3.5 Sv. With ongoing spinup the overflow transport is decreasing from L1 to L5 and from H1 to H5 by ~0.3 Sv and ~0.6 Sv, respectively. There is a larger variability on interannual time scales in the high-resolution model including periods of weaker (e.g., late 1960s and late 1970s) and stronger (e.g., mid-1970s, mid-1980s, and 2000s) transports in H5 compared to L5. In the late 1990s, H5 exhibits a pronounced deep overflow increase of ~1 Sv in a few years, followed by a slower ~0.75 Sv decrease in the years 2000–10 (the ~0.75 Sv reduction is also seen in the low-resolution model). This rather steep overflow increase is somewhat weaker in the observations of Jochumsen et al. (2017) (black solid line) and accompanied by a much larger variability. The high-resolution overflows are in the range of the

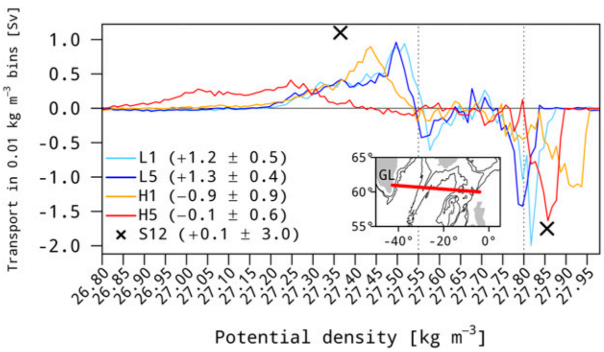

FIG. 9. Average summer (June–July, 2002–08) transports (Sv; integrated in 0.01 kg m^{-3} bins; positive northward) across ~60°N in the eastern North Atlantic (red line in inset; black lines show 1- and 2-km isobaths). Black crosses show density and strength of observed maximum northward and southward transports (Sarafanov et al. 2012). Dashed vertical lines indicate the observed boundaries between upper northward ($\sigma_\theta < 27.55$ kg m^{-3}), deep southward ($\sigma_\theta > 27.8$ kg m^{-3}), and intermediate waters in between. Numbers in parentheses show net transport across the section and uncertainties (Sv; given by authors for the observation and one standard deviation of this 14-month period for the models). Note that the shape and strength of the modeled transports does not change significantly if the annual long-term average (January–December, 1961–2009) is used.

observations being approximately in the upper (H5) and lower (H1) bounds of the observed variability (20-day low-pass-filtered measurements, gray line in Fig. 10). Taking the deep overflow over the Greenland shelf into account (i.e., the full transport across Denmark Strait, dashed lines in Fig. 10), additional ~0.5–1 Sv are transported southward. In general, no further temporal variability is added if the whole cross section is considered compared to the section from Iceland to 29°W. In H5, however, the eastern branch (from Iceland to 29°W) contributes almost entirely to the total overflow during phases of low overflow (e.g., late 1960s and late 1970s), which is not the case in H1.

Neither significant trends nor a seasonal cycle exist in the Denmark Strait overflow observations between 1996 and 2016 (Fig. 10b). Linear trends between 1996 and 2009 of the modeled dense overflow (monthly time series) exhibit small p values, indicating a significant trend. However, the corresponding coefficients of determination R^2 are all close to zero, which is why we reject the hypothesis that there are statistical significant trends (not shown). The high-resolution modeled overflow transport indicates a clear seasonal cycle with a maximum transport in winter and a minimum transport in summer (Fig. 10b). With ongoing spinup, the H5 run shows an enhanced transport in February, March, and October and a minimum around June. The seasonal cycle of the overflow transport in L1 and L5 indicates a much weaker variability and resembles better the negligible seasonal cycle of the observed overflow data but at a transport strength that is around 1 Sv weaker than the observed one.

Further downstream the WBC leaves the Irminger Sea southward along the Greenland coast. Figure 11 shows the southward flow across ~60°N decomposed in the upper light ($\upsilon < 0$ m s^{-1}, $\sigma_\theta < 27.8$ kg m^{-3}) East Greenland/Irminger Current (EGIC) and the lower deep ($\upsilon < 0$ m s^{-1}, $\sigma_\theta > 27.8$ kg m^{-3}) WBC (DWBC) in summer (June–July, 2002–08) integrated from South Greenland until 38°W. In both models the DWBC transport decreases in favor of

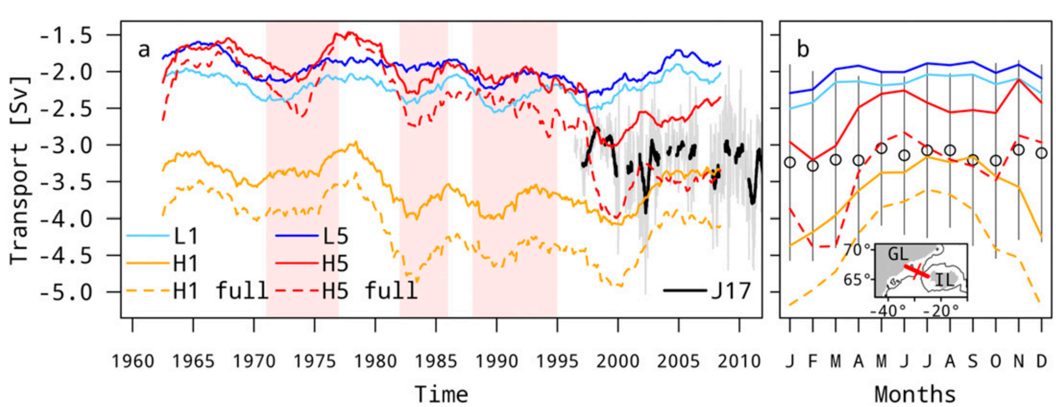

FIG. 10. Deep overflow (Sv; negative southward; $\sigma_\theta > 27.8$ kg m^{-3}) across Denmark Strait from Iceland to 29°W (solid) and the full section from Iceland to Greenland [dashed, both cross-section locations shown in (b); thin black line shows 500-m isobath]. (a) Colored lines show 3-yr low-pass-filtered first and fifth low- and high-resolution model results. Gray (black) line shows 20-day (6-month) low-pass-filtered measurements of Jochumsen et al. (2017). (b) Average (1996–2009) annual cycle of deep overflow. Black circles and lines show the mean and one standard deviation of the observations. Red bars in (a) show deep Labrador Sea MLD periods of the H5 spinup (Fig. 15b).

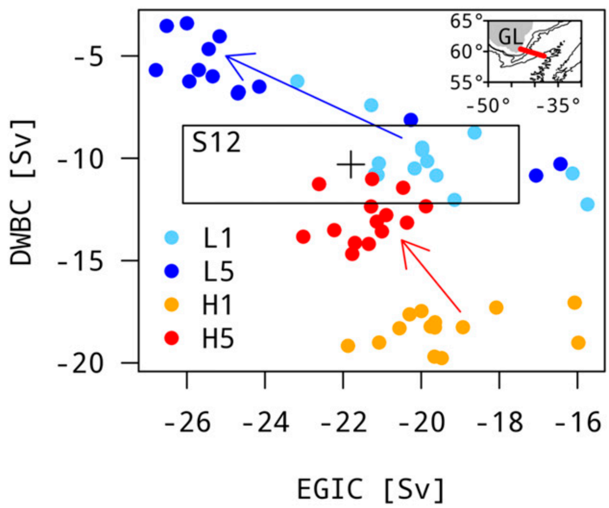

FIG. 11. Monthly summer (June–July, 2002–08) transports (Sv; southward negative) of the EGIC ($\sigma_\theta < 27.8\,\mathrm{kg\,m^{-3}}$) and DWBC ($\sigma_\theta > 27.8\,\mathrm{kg\,m^{-3}}$) across ~60°N from southern Greenland until 38°W (red line in inset; black lines show 1-, 2-, and 3-km isobaths). Colored arrows show transition from first to fifth spinups of low- (blue) and high-resolution (red) model runs. The black cross and box show the mean and uncertainty of observations from (Sarafanov et al. 2012) for the same time period and location. Note that the shape of the modeled transports does not change significantly if the annual long-term average (January–December, 1961–2009) is used.

the EGIC from the first to fifth spinup (due to colder and fresher conditions, not shown). In L5, the resulting DWBC transport is weaker than observed (black cross and box; Sarafanov et al. 2012). In H5, in contrast, both the EGIC and DWBC are in the range of observations after an initial too strong DWBC in the H1 run. Note that these density distributions do not change the general results if the long-term average (January–December, 1961–2009) is used (not shown).

c. Labrador Sea mixed layer restratification

Figure 12 shows the water mass properties as a function of depth in the central Labrador Sea temporally and horizontally averaged over the period 1965–2004 and the index area shown in Figs. 1 and 13. Both models show in general denser waters than observed in almost the entire water column [Figs. 12a,d; *WOA13* from Locarnini et al. (2013) and Zweng et al. (2013), blue crosses; EN4 from Good et al. (2013), version 4.2.1, black dashed line]. The dense biases reduce from the first to the fifth spinup due to colder (Figs. 12b,e) and fresher (Figs. 12c,f) conditions. In the upper ~100 m, H5 is the only run where the density as well as the salinity lie in the observed range (Figs. 12a,c) although a notable cold water patch exists at the subsurface (~50–150 m; Fig. 12b). This patch is absent in the L1 and H1 runs and weaker in L5. All other runs than H5 are too salty and too dense and exhibit a weaker stratification compared to observations. At middepth, L5 is closest to the observed salinity range, while all other model runs being too salty (Fig. 12f). Below 2500 m, all models exhibit a warm bias (Fig. 12e) that leads to lighter waters than observed (Fig. 12d).

The average March (1961–2009) modeled North Atlantic MLD, defined as the depth at which the potential density deviates from the 10 m depth value by $\Delta\sigma_\theta = 0.125\,\mathrm{kg\,m^{-3}}$ (Monterey and deWitt 2000; Danabasoglu et al. 2014), is confined to two areas: the Labrador Seas and the Nordic Seas (Fig. 13). Observed (EN4; Good et al. 2013; Fig. 13a) and modeled winter MLDs are very deep (>3000 m and up to bottom) in the Labrador Sea and shallower (~2000 m) in the Nordic Seas. A longer model spinup leads to shallower MLDs in the high-resolution model (Fig. 13d). The low-resolution MLD, in contrast, remains rather unchanged after five spinups (Fig. 13c; differences to L1 are negligible and not shown).

The average March (1979–2009) sea ice concentration (%) as modeled (solid lines) and observed (dashed lines, NSIDC; Cavalieri et al. 1996) is added to Fig. 13. In both models the 15 and 50% sea ice concentrations generally resemble those observed (Figs. 13c,d). However, both models underestimate the sea ice concentration in the Labrador Sea. L5, in addition, overestimates the 15% sea ice concentration in the Nordic Seas. A distinct sea ice change in the Nordic Seas is visible between the H1 and H5 runs, where the sea ice extent decreases with spinup time. Especially the 50% sea ice concentration is reduced in H5 and underestimates the one observed.

The March sea ice extent evolution in the Nordic Seas and the Labrador Sea is shown in Fig. 14 (total area with sea ice concentration > 15%; $\mathrm{km}^2 \times 10^4$). In both domains periods of lesser and greater sea ice extent are visible. In the Labrador Sea, periods of increased sea ice extent are in line with the modeled deep convection activity, indicated by red bars in Fig. 15b. The high-resolution model exhibits a transition from the first to the fifth spinup: while the sea ice extent decreases in the Nordic Seas (Fig. 14a), an increase is visible in the Labrador Sea especially during periods of deep convection (mid-1970s, mid-1980s, early to mid-1990s; Fig. 14b). In both domains, this spinup transition yields sea ice extent as observed in the H5 run (black lines, NSIDC; Cavalieri et al. 1996). The low-resolution model, in contrast, overestimates (underestimates) the sea ice extent in the Nordic Sea (Labrador Sea) and the spinup transition seen in the high-resolution model is almost absent.

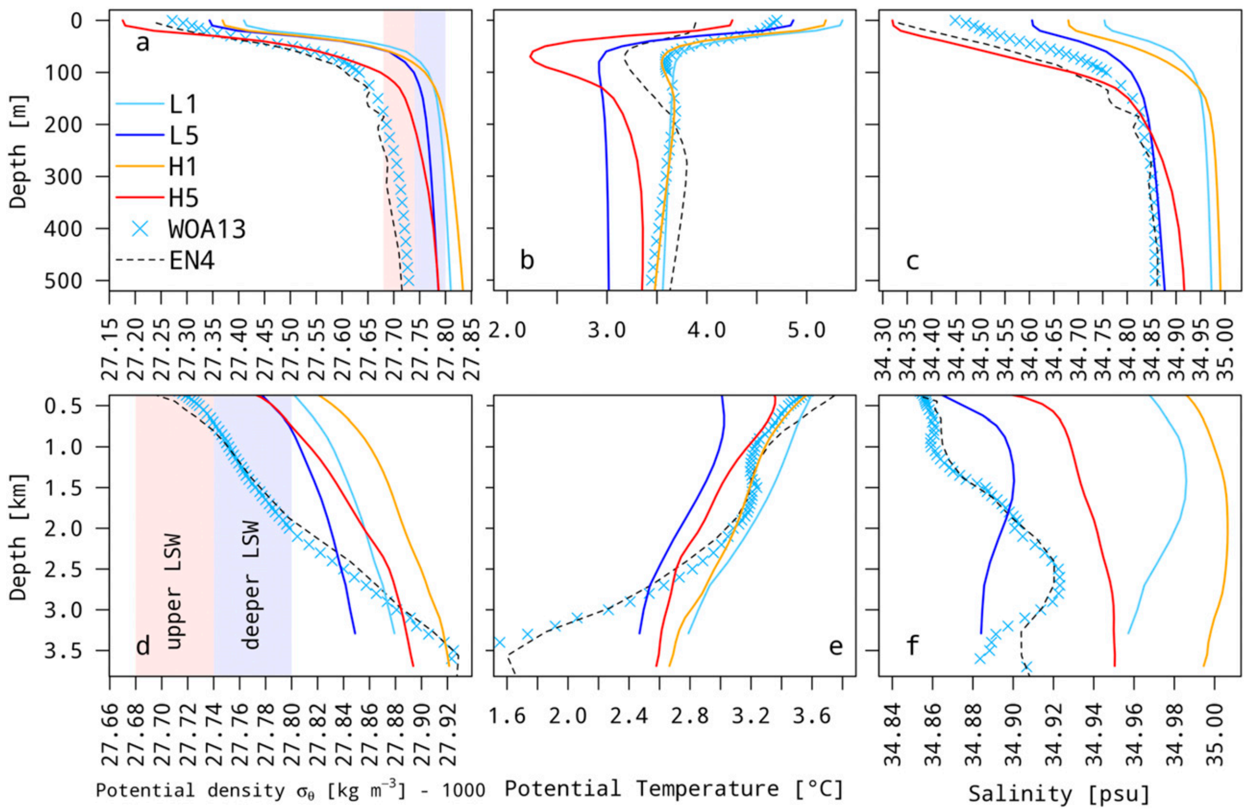

FIG. 12. Average (1965–2004) upper 500-m (top row) and deeper (lower row) (a),(d) potential density σ_θ (kg m^{-3} − 1000), (b),(e) potential temperature (°C), and (c),(f) salinity (psu) in the central Labrador Sea (white polygons in Fig. 13). Observations are from Locarnini et al. (2013) and Zweng et al. (2013) (both *WOA13*; blue crosses) and Good et al. (2013) (EN4; black dashed line) averaged over the same time period and area and linearly interpolated to regular depth levels. Red and blue shading in (a) and (d) shows upper and deeper (or classical) Labrador Sea Water density ranges.

The decadal variability of the average March MLD in the Labrador Sea is shown in Fig. 15 (index areas indicated in Figs. 1 and 13). The modeled low-resolution winter MLD remains at great depths (~3 km) throughout the entire simulated period and do not change with the number of spinup cycles (Fig. 15a). In the high-resolution model, in contrast, a large interannual variability evolves with an increasing number of spinup cycles (Fig. 15b). After 3 spinups, periods of shallow MLDs (e.g., late 1960s, around 1980, around 2005) are visible between periods of deep MLDs (e.g., early 1970s, around 1984, early 1990) indicating a restratification of the mixed layer. This restratification is also visible in the observations (black crosses in Fig. 15, calculated based on the EN4, Good et al. (2013) with the same MLD criterion). Note that different maximum depths in the area yield different maximum MLDs compared to the models.

The average winter (January–March, 1965–2004) Labrador Sea hydrography is shown in Fig. 16. Similar to the annual mean (Fig. 12), a transition toward lighter waters is seen from the first to the fifth spinups in both models (Fig. 16a) through colder (Fig. 16b) and fresher conditions (Fig. 16c). In particular the upper-ocean pycnocline of the H5 run (red line in Fig. 16a) is shallower and covers a wider density range compared to all other model runs, caused by fresh waters. Below 1-km depth the L5 run exhibits lighter conditions compared to all other runs, also caused by a lower salinity.

4. Discussion

Decreasing the horizontal model grid size down to the order of the first baroclinic deformation radius [O(1–10) km; e.g., Chelton et al. 1998] yields stronger and narrower currents with vigorous meanders in the North Atlantic Ocean compared to the low-resolution control experiment with a typical ~1° ≈ 100-km resolution. The strength, position, and shape of the circulation in the H1 run generally resemble observations better (e.g., AMOC and total meridional oceanic heat transport; Figs. 5, 6). The correct position of strong

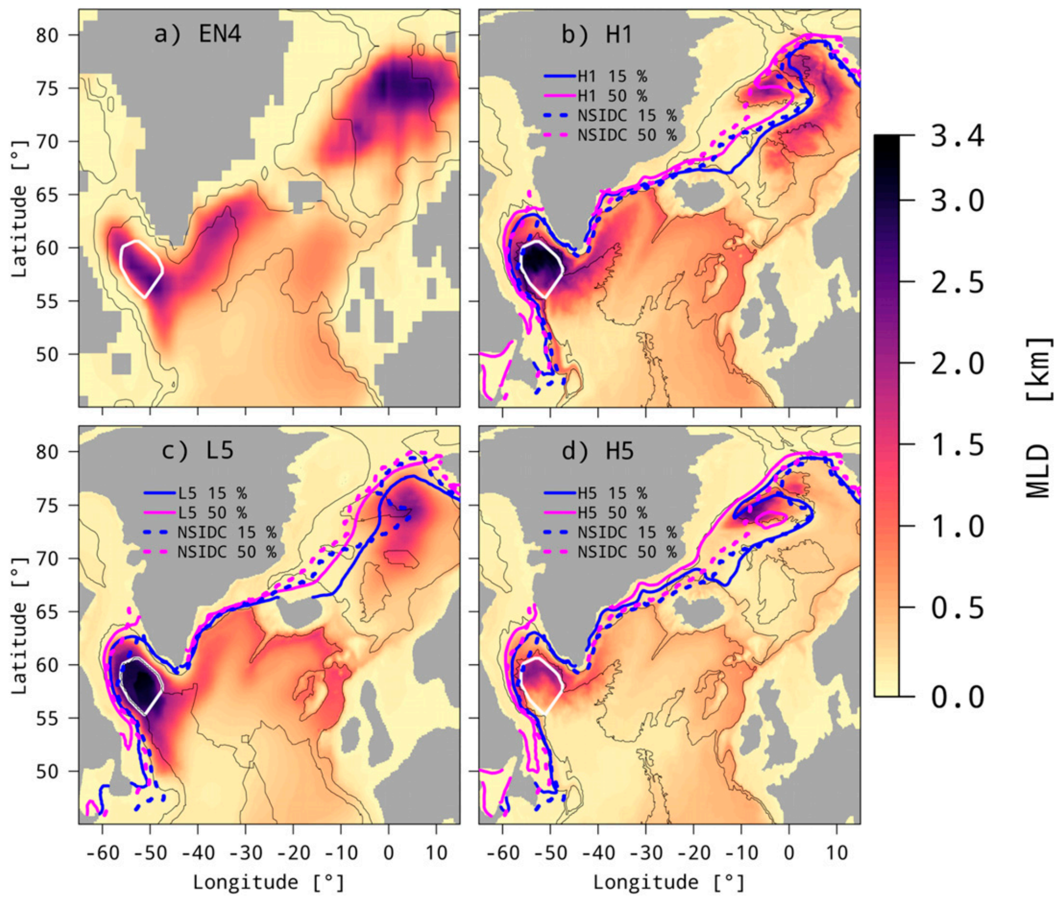

FIG. 13. Average (1961–2009) March MLD (km; defined as the depth at which the potential density σ_θ deviates from its 10-m depth value by 0.125 kg m^{-3}) of (a) EN4 observations (Good et al. 2013), (b) first high-, and (c),(d) fifth low- and high-resolution spinups, respectively. Thin black lines are 1- and 3-km isobaths. Thick white polygons enclose the 3-km low-resolution model bathymetry in the Labrador Sea interior that is used for area averaging. Blue and magenta lines show the average (March, 1979–2009) 15% and 50% sea ice concentration as modeled (solid) and measured (dashed) by satellites (NSIDC; Cavalieri et al. 1996). MLD differences between L1 and L5 are negligible and are not shown.

currents such as the Gulf Stream and North Atlantic Current (Fig. 7b) leads to distinct improvements of the upper-ocean hydrography with respect to observations (Fig. 8b). Similar improvements were observed in other high-resolution ocean modeling studies (e.g., Hurlburt and Hogan 2000; Treguier et al. 2005; Bryan et al. 2007; Talandier et al. 2014; Marzocchi et al. 2015).

However, in both models (low and high resolution) the intermediate and deep circulation needs several spinup cycles (~150–300 years) to develop (Figs. 4, 5). During this spinup time the position of strong currents is not maintained in the high-resolution model and its positive effects seen in the H1 run partially vanish. In fact, H5 resembles the low-resolution control run L5 in terms of a too zonal Gulf Stream extension (Fig. 7) and upper-ocean hydrographic biases (Fig. 8). This unexpected result was not seen in other high-resolution ocean modeling studies due to their rather short simulation lengths O(1–20) years (Treguier et al. 2005; Bryan et al. 2007; Rattan et al. 2010; Talandier et al. 2014; Marzocchi et al. 2015; Dupont et al. 2015; Hewitt et al. 2016; Iovino et al. 2016). For example, Marzocchi et al. (2015) found similar hydrographic improvements in the North Atlantic using a 1/12° configuration of the ocean model ORCA in a 30-yr-long simulation compared to a 1° control run (cf. their Figs. 4a,c with Figs. 8a,b).

The model biases in NAC and associated North Atlantic hydrography are also seen in other high-resolution ocean modeling studies (e.g., Sein et al. 2017). The incorporation of atmosphere–ocean corrections (Weese and Bryan 2006) or feedbacks (Renault et al. 2016), on the other hand, yield realistic current paths and reduced hydrographic biases in ocean-only models. However, similar biases are known problems also in

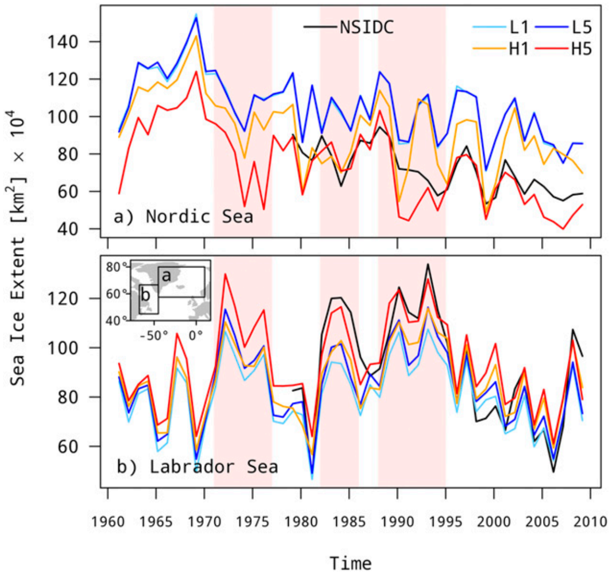

FIG. 14. March sea ice extent (total area with sea ice concentration > 15%; $km^2 \times 10^4$) in (a) Nordic Sea and (b) Labrador Sea basins [summation areas are shown in (b)]. NSIDC (black line) are satellite observations from Cavalieri et al. (1996). Red bars show deep Labrador Sea MLD periods of the fifth H5 spinup (Fig. 15b).

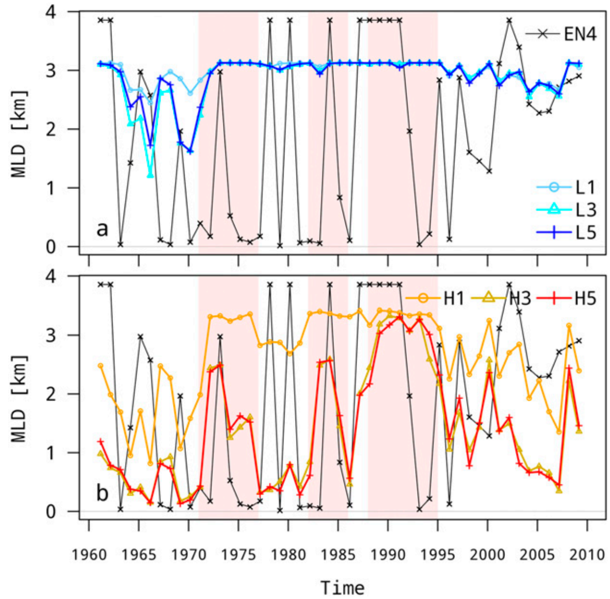

FIG. 15. Decadal variability of average March MLD (km; defined as the depth at which the potential density σ_θ deviates from the 10-m depth value by $0.125\,kg\,m^{-3}$; central Labrador Sea as indicated in Figs. 1 and 13) as modeled by (a) low- and (b) high-resolution models and observed [black; derived from EN4 data (Good et al. 2013) with the same MLD criterion as used in the models; identical in (a) and (b); different maximum depths in the area yield different maximum MLDs compared to models]. Note that (a) and (b) have the same y axis. Red bars show deep Labrador Sea MLD periods of the H5 spinup.

coupled atmosphere–ocean GCMs (C. Wang et al. 2014; Menary et al. 2015). C. Wang et al. (2014) attribute the cold bias to an AMOC reduction. We do see the same relationship (Figs. 5, 8), however, it remains unclear why the position of the NAC is not stable throughout the spinup cycles.

Earlier studies found that the ocean model adjustment for Kelvin and Rossby waves strongly depends on the model resolution and viscosity, respectively (Cherniawsky and Mysak 1989). In our high-resolution model, vertical displacements of several tens of meters magnitude propagate through the thermocline with a westward velocity of $3.12 \pm 0.07\,cm\,s^{-1}$ (Fig. 3b; similar patterns of several cm magnitude exist in the modeled high-resolution SSH field, not shown). In accordance with midlatitude long planetary wave theory as well as observations we identify these propagations as long baroclinic Rossby waves (Kessler 1990; Chelton and Schlax 1996; Chelton et al. 1998) and as a potential cause for the relatively strong upper-ocean adjustment during the high-resolution model spinup. For example, the westward thermocline propagation identified in Fig. 3, representing the first baroclinic mode, would need around 8 years to cross the Atlantic (at 30°N the Atlantic basin width measures approximately 7891 km in both models). According to theory, long baroclinic Rossby waves with increasing vertical wavenumbers m, each traveling with a velocity $c_{R,m} = -\beta\lambda_{R,m}^2 \overset{\text{WKB}}{\approx} m^{-2}\left\{-\beta\left[(f\pi)^{-1}\int_{-H}^{0} N(z)\,dz\right]^2\right\}$ where the mth baroclinic (or internal) Rossby radius of deformation $\lambda_{R,m} = c_{g,m}|f|^{-1}$ for latitudes $\phi \geq 5°$ with Coriolis parameter f and its meridional change $\beta = \partial_y f$, would exhibit a reduced speed by the factor m^{-2} (Chelton et al. 1998; a negative velocity indicates a westward directed Rossby wave). This implies that the associated second and third baroclinic modes already need around 32 and 72 years, respectively, to cross the Atlantic Ocean. In our model comparison we find that spatiotemporal propagation patterns of the first two baroclinic horizontal velocity modes R_1 and R_2 are of much larger amplitude in the high- compared to the low-resolution model (Fig. A4; see section 3a for details). Hence, in accordance with, for example, Cherniawsky and Mysak (1989), Chelton and Schlax (1996), Wunsch (1997), and Clément et al. (2014), we argue that long baroclinic Rossby waves modify the upper-ocean circulation and thereby lead to a stronger adjustment of the high-resolution upper ocean throughout the spinup cycles. In this context two technical aspects may need to be considered: 1) the unphysical jump, which is introduced at the beginning of every consecutive forcing cycle, may affect the wave propagation mechanism (Griffies et al. 2012) and 2) the large differences between the horizontal resolutions also affect the strength the applied SGS closures for momentum and tracers. In areas of

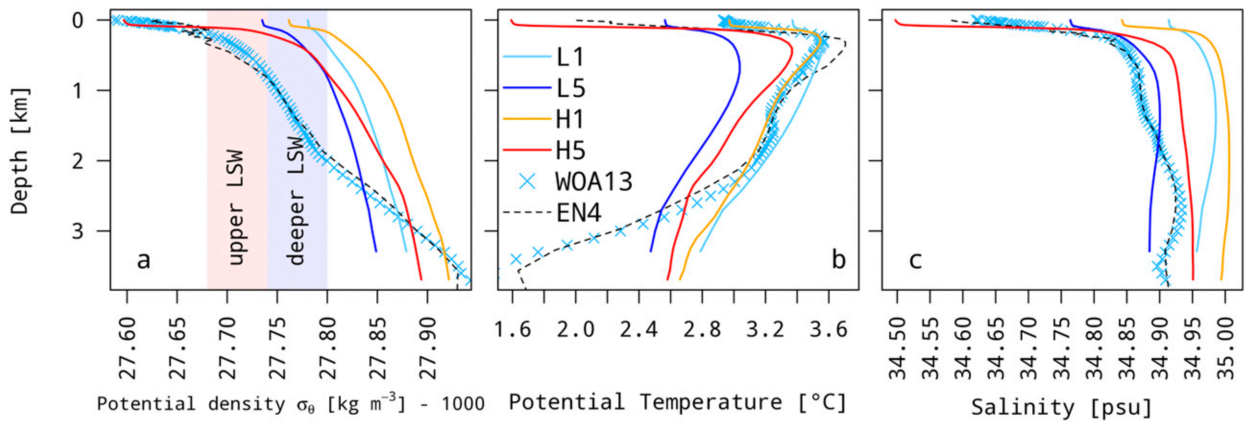

FIG. 16. As in Fig. 12, but for winter (January–March).

mesh refinement the average (1948–2009) depth-integrated SGS temperature flux is smaller by several orders of magnitude in the high- compared to the low-resolution model (cf. Fig. 1 with Fig. A2; SGS temperature flux in °C m^2 s^{-1}; the product of the eddy-induced velocity $\mathbf{u}_{\mathrm{SGS},h}$ and potential temperature T was calculated at every model time step). However, a detailed analysis of this relationship is beyond the scope of this study.

While the correctly modeled surface circulation (position and strength) of the H1 run is not maintained throughout the spinup cycles, a pronounced decadal variability of deep convection evolves in the Labrador Sea (Fig. 15b), similarly to the one derived from observational EN4 data (Good et al. 2013). This variability is nearly absent in the low-resolution model and in H1 (and H2): these runs show deep winter mixed layers through the whole forcing period (Fig. 15a). Too deep winter MLDs are a typical problem of ocean general circulation models (Oschlies 2002; Fox-Kemper et al. 2008; Danabasoglu et al. 2014, 2016; Heuzé 2017) due to wrong current pathways, an insufficient vertical resolution, unresolved mixing processes but also an ill-defined mixed layer depth (usually via property difference to surface) through, for example, temperature–salinity compensation (Courtois et al. 2017).

Observations and models show a primarily wind-driven temporal variability of Labrador Sea deep convection (Kieke et al. 2007; Rhein et al. 2011; Yashayaev and Loder 2017; Scaife et al. 2014; Ortega et al. 2017). Since we use the same atmospheric forcing in all our model runs, we can conclude that the mean Labrador Sea hydrography is responsible for the agreement between the high-resolution modeled and observed MLD (Figs. 13, 15b). Only in the H5 run the slope of the winter (January–March) pycnocline is shallow enough (Fig. 16a) to cover a density range large enough that the traditional MLD definition is meaningful [here via a potential density σ_θ difference of 0.125 kg m^{-3} (Monterey and deWitt 2000; Danabasoglu et al. 2014); see, e.g., Holte and Talley (2009) and Courtois et al. (2017) for an improved MLD definition based on linear fits of the full set of water mass properties, i.e., temperature, salinity, and density].

These lighter water masses in the Labrador Sea in the H5 run (Figs. 12, 16) originate from the southeastward shifted NAC that is more zonal (Figs. 2, 7), weaker (the maximum overturning at 41°N is reduced toward observations; Fig. 5b) and transports lighter water masses across ~60°N northward (Fig. 9) compared to all other model runs. As a consequence, the southward directed Denmark Strait overflow is strongly reduced from H1 to H5, but still being in the observed range (Fig. 10; Jochumsen et al. 2017). The low-resolution Denmark Strait overflow, in contrast, is clearly weaker than observed albeit the relatively high horizontal resolution of ~15 km at the Denmark Strait (Fig. 1a). This adaption of the deep overflow water with respect to lighter source

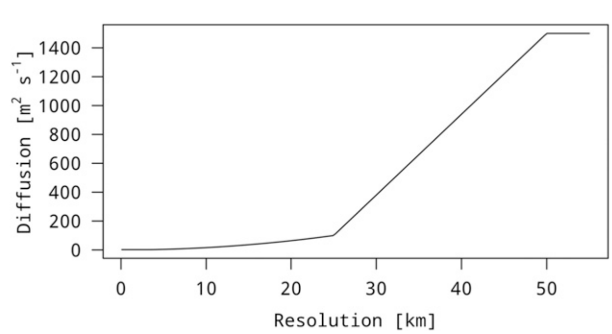

FIG. A1. SGS flux scaling with horizontal resolution (km) as applied in both low- and high-resolution models. The scaling is limited by 2 m^2 s^{-1} at the lower end and the background horizontal diffusion $K_{h,0}$ = 1500 m^2 s^{-1} above 50-km local horizontal resolution (for details, see Q. Wang et al. 2014).

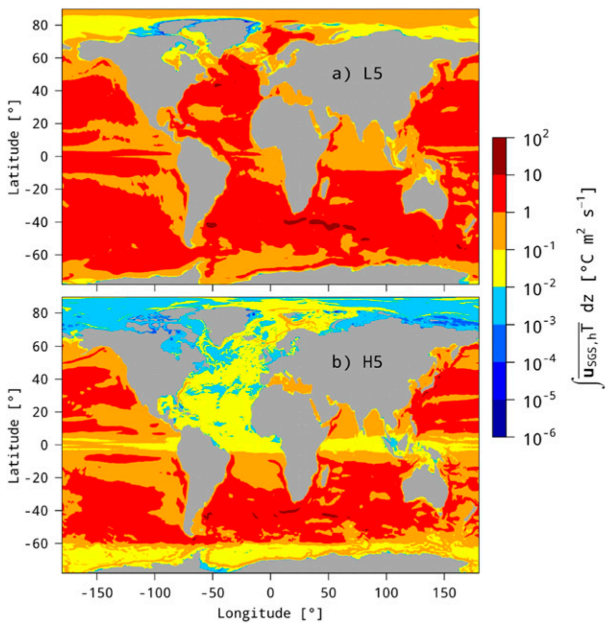

FIG. A2. Average (1948–2009) depth-integrated horizontal SGS temperature flux (°C m^2 s^{-1}) of fifth spinups of (a) low- and (b) high-resolution models. Note the logarithmic color scale. The product of the eddy-induced velocity $\mathbf{u}_{SGS,h}$ and potential temperature T was calculated at every model time step.

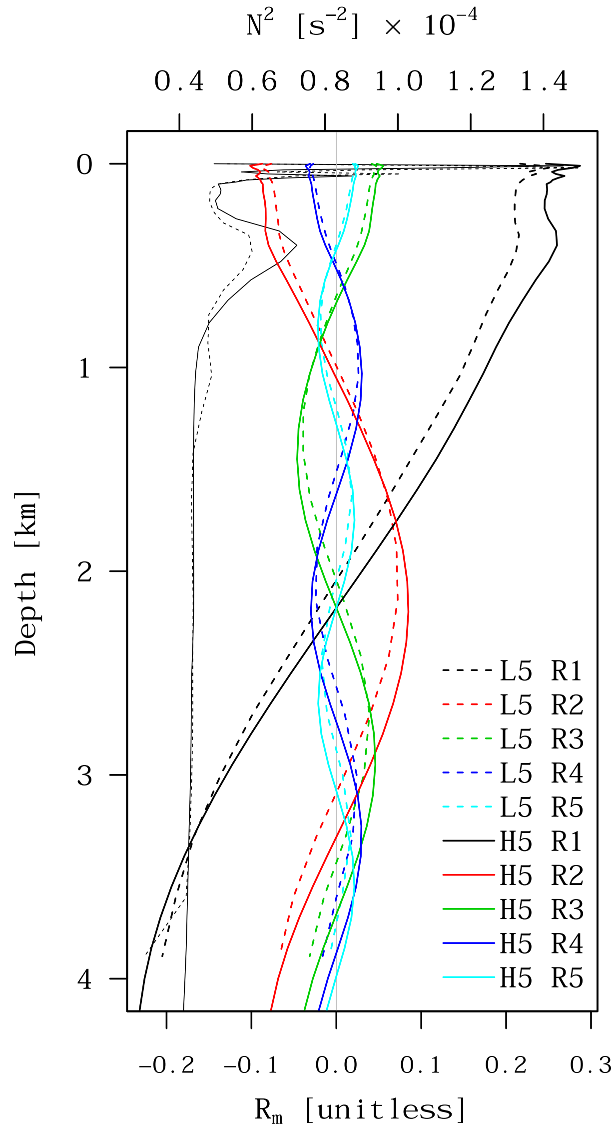

FIG. A3. Exemplary stratification $N^2 = g\rho^{-1}\partial_z\rho$ (s^{-2} × 10^{-4}; upper axis; thin black lines) and associated first five WKB approximated baroclinic horizontal velocity mode amplitudes R_m (unitless; lower axis) of the fifth spinups of the low- (dashed) and high-resolution (solid) models in the North Atlantic at 47.4°N, 20°W of the modeled year 1983 (see description of Fig. 3 in section 3a for details).

water was also observed in Zhang et al. (2011). Further downstream the WBC leaves the Irminger Sea southward consisting of ~70% upper EGIC ($\sigma_\theta < 27.8$ kg m^{-3}) and ~30% DWBC ($\sigma_\theta > 27.8$ kg m^{-3}) as observed during summer (June–July) 2002–08 (Sarafanov et al. 2012; black cross and box in Fig. 10). This water mass distribution is represented in the H5 run after a transition from too dense waters in H1 (red arrow in Fig. 10). The DWBC transport decreases by ~30% (from ~19 to ~13 Sv) as the lighter EGIC transport slightly increases. This transition also exists in the low-resolution model (~50% reduction of DWBC from L1 to L5), however, in L5, the WBC is too light (blue arrow in Fig. 10).

In addition, the southeastward shift of the NAC from the H1 to the H5 run affects the Nordic Sea and Labrador Sea maximum (March) sea ice extent. While the models agree in the general spatial distribution (Fig. 13, blue and magenta solid and dashed lines), they generally overestimate (underestimate) the sea ice extent in the Nordic Sea (Labrador Sea) basins (Fig. 14). It is the H5 run that shows agreement with satellite observations in both basins (Cavalieri et al. 1996). The sea ice reduction in the Nordic Sea from H1 to H5 on the one hand and the increase in the Labrador Sea on the other results from the southeastward shift of the NAC (Figs. 7b,d). In quasi equilibrium, the NAC transports warm waters into the Nordic Seas across the sill between Iceland and Scotland which leads to a warm upper-ocean temperature bias (Fig. 8f) that reduces the overestimated sea ice of the H1 run (Fig. 14a). At the same time the amount of heat transported along Reykjanes Ridge into the Labrador Sea decreases, which leads to increased sea ice extent there (Fig. 14b).

Hence, in our high-resolution model, the interplay of a long spinup adjustment and the large-scale circulation in the North Atlantic subpolar gyre seems to

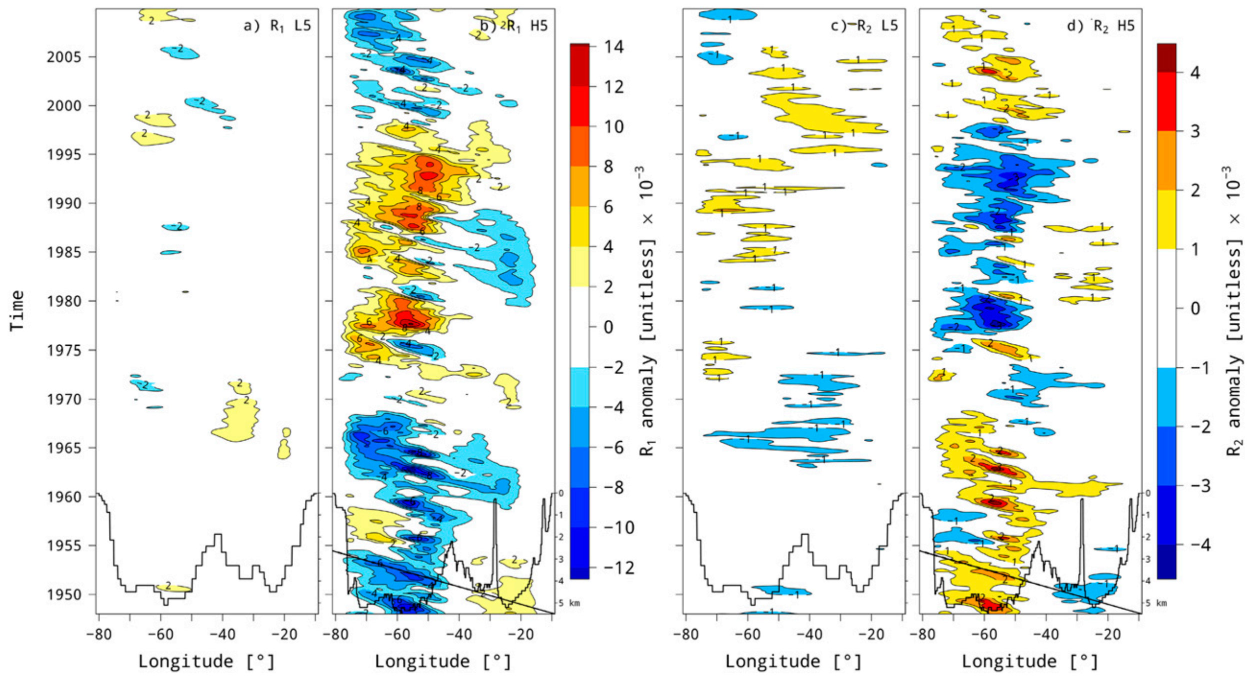

FIG. A4. Anomalies of the (left) first and (right) second WKB approximated baroclinic horizontal velocity mode amplitudes R_1 and R_2 at 500-m depth of the fifth spinups of (a),(c) low- and (b),(d) high-resolution models as a function of longitude and time along 30°N in the Atlantic (colors; unitless × 10^{-3}; seasonal mean 1948–2009 removed). The anomalies were smoothed with a Gaussian Nadaraya–Watson filter with a bandwidth of 3° in the longitudinal direction. The model bathymetry is added as black line [km; axes on the lower right of (b) and (d)]. The straight black and dotted lines in (b) and (d) show a westward velocity of 3.4 ± 0.02 cm s^{-1} as determined by Radon transform performed in the area west of the MAR (see description text of Fig. 3 in section 3a for details).

reduce typical model biases related to a salinification (Treguier et al. 2005; Brandt et al. 2007; Chanut et al. 2008; Rattan et al. 2010; Xu et al. 2013; Marzocchi et al. 2015) and a too deep mixed layer depth in the Labrador Sea (Oschlies 2002; Fox-Kemper et al. 2008; Danabasoglu et al. 2014, 2016; Heuzé 2017).

5. Conclusions

With the global coupled finite element sea ice–ocean model FESOM we investigated the influence of a regionally increased resolution up to 5–15 km on the North Atlantic Ocean circulation and hydrography. Compared to our low-resolution (~1°) control run, this high horizontal resolution leads to distinct improvements of the modeled oceanic circulation and water mass characteristics such as correctly positioned strong and narrow boundary currents, vigorous small-scale meanders and reduced upper-ocean hydrographic biases. Similar improvements were found in earlier studies (e.g., Hurlburt and Hogan 2000; Treguier et al. 2005; Bryan et al. 2007; Talandier et al. 2014; Marzocchi et al. 2015).

However, we find that in our high-resolution model configuration, the upper-ocean circulation changed considerably throughout the first three spinup cycles (~180 model years) before reaching a quasi-equilibrium state. During that spinup, a southeastward shift of the NAC decreases the upper-ocean heat and salt transports into the Labrador Sea, leading to a reduced subpolar gyre salinification, shallower winter mixed layer depths in the Labrador Sea as well as a realistic sea ice extent. This adjustment of the upper-ocean circulation was much weaker in our ~1° control run. On the other hand, in quasi equilibrium, the high-resolution model exhibits similar biases seen in the low-resolution model such as a too weak overturning and a pronounced North Atlantic upper-ocean cold bias through the misplaced NAC.

We assume that the ocean adjustment is different for high and low model resolutions due to different representations of long baroclinic Rossby waves, consistent with earlier studies (Cherniawsky and Mysak 1989). Slow westward wave propagations may be responsible for altering the modeled upper-ocean dynamics on a decadal time scale in the high-resolution model as they are nearly absent in the low-resolution control run. Further research is necessary to identify the influence of baroclinic wave dynamics on the ocean model spinup adjustment.

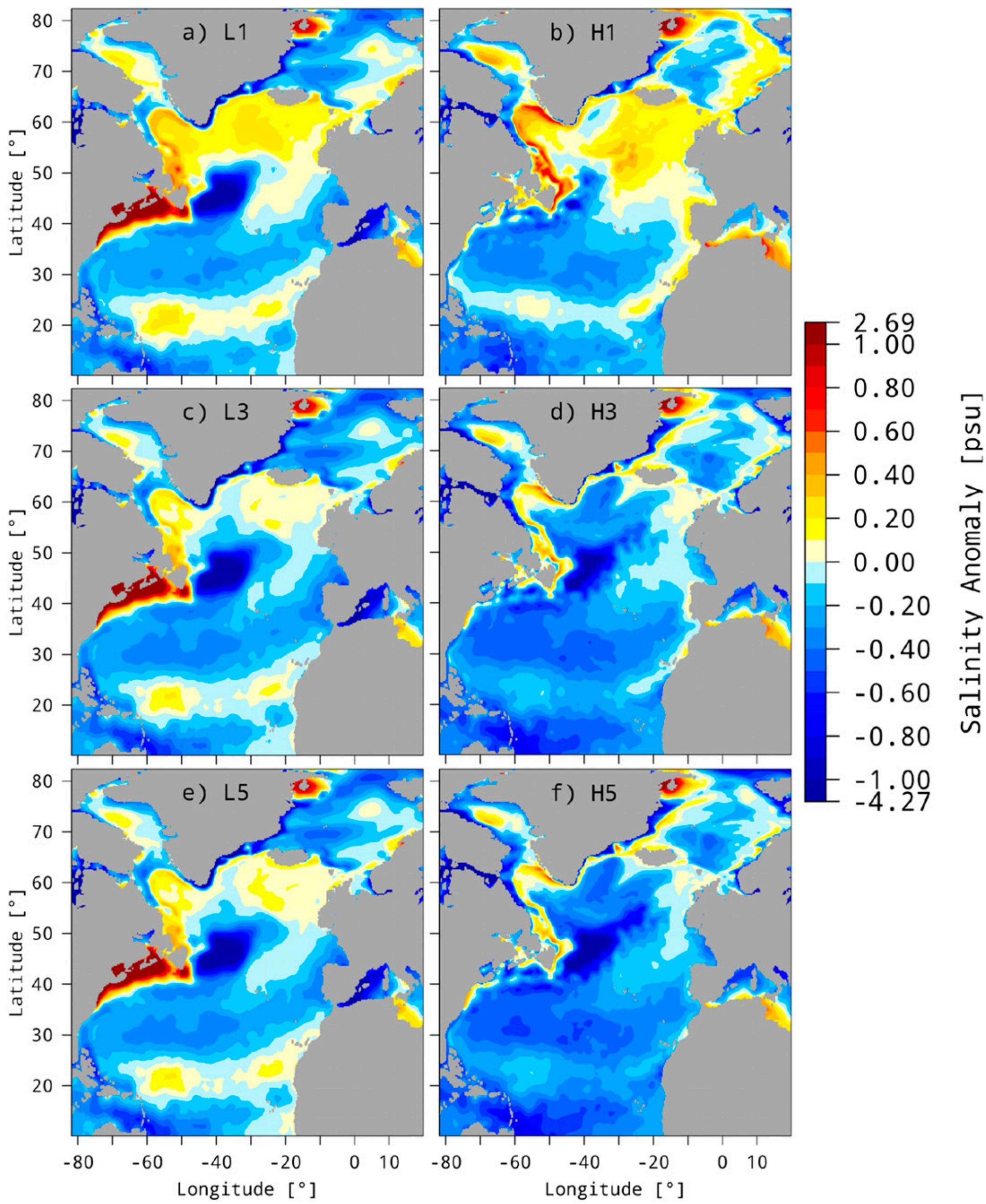

FIG. A5. Average (1965–2004, 0–100 m) salinity anomalies (model minus observation; psu) of (left) low- and (right) high-resolution models. Observations are from *WOA13* (Zweng et al. 2013). Anomalies of (a),(b) first, (c),(d) third, and (e),(f) fifth model spinup minus observations.

Our study highlights the need of a spinup long enough to bring the model in a quasi-equilibrium state if a high horizontal resolution is used. With our current technology we are approaching high-resolution model studies in climate models (e.g., Haarsma et al. 2016; Hewitt et al. 2016). Our results suggest that such experiments should be carefully compared to known low-resolution GCM deficits (C. Wang et al. 2014; Menary et al. 2015). As a logical next step, we will evaluate the spinup dynamics in coupled climate models.

Acknowledgments. This work was funded through MARUM DFG project, "The Ocean in the Earth System" (Grant FZT 15/4) which is part of the Excellence Cluster Initiative (309/2) and the MARUM project OC1, "Changes in large-scale overturning circulation: Present and past." The altimeter products were produced by Ssalto/Duacs and distributed by Aviso, with support from Cnes, http://www.aviso.altimetry.fr/duacs/). We thank three anonymous reviewers whose comments have greatly improved this manuscript.

APPENDIX

Appendix Figure Details

In our model simulations, the strength of the parameterized tracer mixing and advection is scaled (among others) with the local horizontal model resolution (section 2). For clarity, this resolution dependence is shown in Fig. A1, and the obtained total depth-integrated subgrid scale (SGS) temperature flux for both low- and high-resolution models is compared in Fig. A2 (°C m^2 s^{-1}); the product of the eddy-induced velocity $\mathbf{u}_{SGS,h}$ and potential temperature T was calculated at every model time step.

Figure A3 exemplarily shows the stratification N^2 and associated WKB approximated horizontal velocity modes $R_{1\text{–}5}$ of the fifth spinups of the low- and high-resolution models in the North Atlantic at 47.4°N and 20°W of the modeled year 1983 (section 3a). In addition, spatiotemporal anomalies (seasonal mean 1948–2009 removed) of R_1 and R_2 along 30°N in the North Atlantic at 500-m depth as a function of longitude and time are shown in Fig. A4.

Complementary to Fig. 8 (section 3b), Fig. A5 shows the average (1965–2004, 0–100 m) salinity anomalies (model minus observation) of our low- and high-resolution models (observations from *WOA13*; Zweng et al. 2013).

REFERENCES

Abe, H., Y. Tanimoto, T. Hasegawa, and N. Ebuchi, 2016: Oceanic Rossby waves over eastern tropical Pacific of both hemispheres forced by anomalous surface winds after mature phase of ENSO. *J. Phys. Oceanogr.*, **46**, 3397–3414, https://doi.org/10.1175/JPO-D-15-0118.1.

Alvera-Azcárate, A., A. Barth, and R. H. Weisberg, 2009: The surface circulation of the Caribbean Sea and the Gulf of Mexico as inferred from satellite altimetry. *J. Phys. Oceanogr.*, **39**, 640–657, https://doi.org/10.1175/2008JPO3765.1.

Amante, C., and B. W. Eakins, 2009: ETOPO1 1 arc-minute global relief model: Procedures, data sources and analysis. NOAA Tech. Memo. NESDIS NGDC-24, accessed 15 July 2015, https://doi.org/10.7289/V5C8276M.

Brandt, P., A. Funk, L. Czeschel, C. Eden, and C. W. Böning, 2007: Ventilation and transformation of Labrador Sea Water and its rapid export in the Deep Labrador Current. *J. Phys. Oceanogr.*, **37**, 946–961, https://doi.org/10.1175/JPO3044.1.

Bryan, F. O., M. W. Hecht, and R. D. Smith, 2007: Resolution convergence and sensitivity studies with North Atlantic circulation models. Part I: The western boundary current system. *Ocean Modell.*, **16**, 141–159, https://doi.org/10.1016/j.ocemod.2006.08.005.

Cavalieri, D. J., C. L. Parkinson, P. Gloersen, and H. J. Zwally, 1996: Sea ice concentrations from Nimbus-7 SMMR and DMSP SSM/I-SSMIS passive microwave data, version 1 (updated yearly). National Snow and Ice Data Center Distributed Active Archive Center, accessed 15 July 2015, https://doi.org/10.5067/8GQ8LZQVL0VL.

Chanut, J., B. Barnier, W. Large, L. Debreu, T. Penduff, J. M. Molines, and P. Mathiot, 2008: Mesoscale eddies in the Labrador Sea and their contribution to convection and restratification. *J. Phys. Oceanogr.*, **38**, 1617–1643, https://doi.org/10.1175/2008JPO3485.1.

Chelton, D. B., and M. G. Schlax, 1996: Global observations of oceanic Rossby waves. *Science*, **272**, 234–238, https://doi.org/10.1126/science.272.5259.234.

——, R. A. deSzoeke, M. G. Schlax, K. E. Naggar, and N. Siwertz, 1998: Geographical variability of the first baroclinic Rossby radius of deformation. *J. Phys. Oceanogr.*, **28**, 433–460, https://doi.org/10.1175/1520-0485(1998)028<0433:GVOTFB>2.0.CO;2.

——, M. G. Schlax, and R. M. Samelson, 2011: Global observations of nonlinear mesoscale eddies. *Prog. Oceanogr.*, **91**, 167–216, https://doi.org/10.1016/j.pocean.2011.01.002.

Cherniawsky, J., and L. Mysak, 1989: Baroclinic adjustment in coarse–resolution numerical ocean models. *Atmos.–Ocean*, **27**, 306–326, https://doi.org/10.1080/07055900.1989.9649338.

Clément, L., E. Frajka-Williams, Z. B. Szuts, and S. A. Cunningham, 2014: Vertical structure of eddies and Rossby waves, and their effect on the Atlantic meridional overturning circulation at 26.5°N. *J. Geophys. Res. Oceans*, **119**, 6479–6498, https://doi.org/10.1002/2014JC010146.

Courtois, P., X. Hu, C. Pennelly, P. Spence, and P. G. Myers, 2017: Mixed layer depth calculation in deep convection regions in ocean numerical models. *Ocean Modell.*, **120**, 60–78, https://doi.org/10.1016/j.ocemod.2017.10.007.

Danabasoglu, G., J. C. McWilliams, and W. G. Large, 1996: Approach to equilibrium in accelerated global oceanic models. *J. Climate*, **9**, 1092–1110, https://doi.org/10.1175/1520-0442(1996)009<1092:ATEIAG>2.0.CO;2.

——, and Coauthors, 2014: North Atlantic simulations in Coordinated Ocean-ice Reference Experiments phase II (CORE-II). Part I: Mean states. *Ocean Modell.*, **73**, 76–107, https://doi.org/10.1016/j.ocemod.2013.10.005.

——, and Coauthors, 2016: North Atlantic simulations in Coordinated Ocean-ice Reference Experiments phase II (CORE-II). Part II: Inter-annual to decadal variability. *Ocean Modell.*, **97**, 65–90, https://doi.org/10.1016/j.ocemod.2015.11.007.

Danilov, S., G. Kivman, and J. Schröter, 2004: A finite-element ocean model: principles and evaluation. *Ocean Modell.*, **6**, 125–150, https://doi.org/10.1016/S1463-5003(02)00063-X.

Dupont, F., and Coauthors, 2015: A high-resolution ocean and sea-ice modelling system for the Arctic and North Atlantic oceans. *Geosci. Model Dev.*, **8**, 1577–1594, https://doi.org/10.5194/gmd-8-1577-2015.

Fan, J., and I. Gijbels, Eds., 1996: *Local Polynomial Modelling and Its Applications*. Monographs on Statistics and Applied Probability, Vol. 66, Chapman and Hall, 360 pp.

Fox-Kemper, B., R. Ferrari, and R. Hallberg, 2008: Parameterization of mixed layer eddies. Part I: Theory and diagnosis. *J. Phys. Oceanogr.*, **38**, 1145–1165, https://doi.org/10.1175/2007JPO3792.1.

Frajka–Williams, E., 2015: Estimating the Atlantic overturning at 26°N using satellite altimetry and cable measurements. *Geophys. Res. Lett.*, **42**, 3458–3464, https://doi.org/10.1002/2015GL063220.

Ganachaud, A., and C. Wunsch, 2003: Large-scale ocean heat and freshwater transports during the World Ocean Circulation Experiment. *J. Climate*, **16**, 696–705, https://doi.org/10.1175/1520-0442(2003)016<0696:LSOHAF>2.0.CO;2.

Gent, P. R., and J. C. McWilliams, 1990: Isopycnal mixing in ocean circulation models. *J. Phys. Oceanogr.*, **20**, 150–155, https://doi.org/10.1175/1520-0485(1990)020<0150:IMIOCM>2.0.CO;2.

Gill, A. E., 1982: *Atmosphere–Ocean Dynamics*. International Geophysics Series, Vol. 30, Academic Press, 662 pp.

Good, S. A., M. J. Martin, and N. A. Rayner, 2013: EN4: Quality controlled ocean temperature and salinity profiles and monthly objective analyses with uncertainty estimates. *J. Geophys. Res. Oceans*, **118**, 6704–6716, https://doi.org/10.1002/2013JC009067.

Griffies, S. M., A. Gnanadesikan, R. C. Pacanowski, V. D. Larichev, J. K. Dukowicz, and R. D. Smith, 1998: Isoneutral diffusion in a *z*-coordinate ocean model. *J. Phys. Oceanogr.*, **28**, 805–830, https://doi.org/10.1175/1520-0485(1998)028<0805:IDIAZC>2.0.CO;2.

——, M. Winton, B. Samuels, G. Danabasoglu, S. G. Yeager, S. J. Marsland, H. Drange, and M. Bentsen, 2012: Datasets and protocol for the CLIVAR WGOMD Coordinated Ocean-sea ice Reference Experiments (COREs). WCRP Informal Rep. 21/2012, 23 pp., http://nora.nerc.ac.uk/id/eprint/500583/.

Haarsma, R. J., and Coauthors, 2016: High Resolution Model Intercomparison Project (HighResMIP v1.0) for CMIP6. *Geosci. Model Dev.*, **9**, 4185–4208, https://doi.org/10.5194/gmd-9-4185-2016.

Han, Z., F. Luo, S. Li, Y. Gao, T. Furevik, and L. Svendsen, 2016: Simulation by CMIP5 models of the Atlantic multidecadal oscillation and its climate impacts. *Adv. Atmos. Sci.*, **33**, 1329–1342, https://doi.org/10.1007/s00376-016-5270-4.

He, Y.-C., H. Drange, Y. Gao, and M. Bentsen, 2016: Simulated Atlantic meridional overturning circulation in the 20th century with an ocean model forced by reanalysis-based atmospheric data sets. *Ocean Modell.*, **100**, 31–48, https://doi.org/10.1016/j.ocemod.2015.12.011.

Heuzé, C., 2017: North Atlantic Deep Water formation and AMOC in CMIP5 models. *Ocean Sci.*, **13**, 609–622, https://doi.org/10.5194/os-13-609-2017.

Hewitt, H. T., and Coauthors, 2016: The impact of resolving the Rossby radius at mid-latitudes in the ocean: Results from a high-resolution version of the Met Office GC2 coupled model. *Geosci. Model Dev.*, **9**, 3655–3670, https://doi.org/10.5194/gmd-9-3655-2016.

Holte, J., and L. Talley, 2009: A new algorithm for finding mixed layer depths with applications to Argo data and Subantarctic Mode Water formation. *J. Atmos. Oceanic Technol.*, **26**, 1920–1939, https://doi.org/10.1175/2009JTECHO543.1.

Hurlburt, H. E., and P. J. Hogan, 2000: Impact of 1/8° to 1/64° resolution on Gulf Stream model–data comparisons in basin-scale subtropical Atlantic Ocean models. *Dyn. Atmos. Oceans*, **32**, 283–329, https://doi.org/10.1016/S0377-0265(00)00050-6.

Ionita, M., P. Scholz, G. Lohmann, M. Dima, and M. Prange, 2016: Linkages between atmospheric blocking, sea ice export through Fram Strait and the Atlantic Meridional Overturning Circulation. *Sci. Rep.*, **6**, 32881, https://doi.org/10.1038/srep32881.

Iovino, D., S. Masina, A. Storto, A. Cipollone, and V. N. Stepanov, 2016: A 1/16° eddying simulation of the global NEMO sea-ice–ocean system. *Geosci. Model Dev.*, **9**, 2665–2684, https://doi.org/10.5194/gmd-9-2665-2016.

Jochumsen, K., M. Moritz, N. Nunes, D. Quadfasel, K. M. H. Larsen, B. Hansen, H. Valdimarsson, and S. Jonsson, 2017: Revised transport estimates of the Denmark Strait overflow. *J. Geophys. Res. Oceans*, **122**, 3434–3450, https://doi.org/10.1002/2017JC012803.

Johns, W. E., and Coauthors, 2011: Continuous, array-based estimates of Atlantic ocean heat transport at 26.5°N. *J. Climate*, **24**, 2429–2449, https://doi.org/10.1175/2010JCLI3997.1.

Karspeck, A. R., and Coauthors, 2017: Comparison of the Atlantic meridional overturning circulation between 1960 and 2007 in six ocean reanalysis products. *Climate Dyn.*, **49**, 957–982, https://doi.org/10.1007/s00382-015-2787-7.

Kessler, W. S., 1990: Observations of long Rossby waves in the northern tropical Pacific. *J. Geophys. Res.*, **95**, 5183–5217, https://doi.org/10.1029/JC095iC04p05183.

Kieke, D., M. Rhein, L. Stramma, W. M. Smethie, J. L. Bullister, and D. A. LeBel, 2007: Changes in the pool of Labrador Sea Water in the subpolar North Atlantic. *Geophys. Res. Lett.*, **34**, L06605, https://doi.org/10.1029/2006GL028959.

Large, W. G., and S. G. Yeager, 2004: Diurnal to decadal global forcing for ocean and sea-ice models: The data sets and flux climatologies. NCAR Tech. Note NCAR/TN-460+STR, 105 pp., https://doi.org/10.5065/D6KK98Q6.

——, and ——, 2009: The global climatology of an interannually varying air–sea flux data set. *Climate Dyn.*, **33**, 341–364, https://doi.org/10.1007/s00382-008-0441-3.

——, J. C. McWilliams, and S. C. Doney, 1994: Oceanic vertical mixing: A review and a model with a nonlocal boundary layer parameterization. *Rev. Geophys.*, **32**, 363–403, https://doi.org/10.1029/94RG01872.

Locarnini, R. A., and Coauthors, 2013: *Temperature*. Vol. 1, *World Ocean Atlas 2013*, NOAA Atlas NESDIS 73, 40 pp., https://www.nodc.noaa.gov/OC5/woa13/pubwoa13.html.

Lohmann, K., H. Drange, and M. Bentsen, 2009: Response of the North Atlantic subpolar gyre to persistent North Atlantic oscillation like forcing. *Climate Dyn.*, **32**, 273–285, https://doi.org/10.1007/s00382-008-0467-6.

Marsh, R., D. Desbruyères, J. L. Bamber, B. A. de Cuevas, A. C. Coward, and Y. Aksenov, 2010: Short-term impacts of enhanced Greenland freshwater fluxes in an eddy-permitting ocean model. *Ocean Sci.*, **6**, 749–760, https://doi.org/10.5194/os-6-749-2010.

Marzocchi, A., J. J.-M. Hirschi, N. P. Holliday, S. A. Cunningham, A. T. Blaker, and A. C. Coward, 2015: The North Atlantic subpolar circulation in an eddy-resolving global ocean model. *J. Mar. Syst.*, **142**, 126–143, https://doi.org/10.1016/j.jmarsys.2014.10.007.

McWilliams, J. C., 1998: Oceanic general circulation models. *Ocean Modeling and Parameterization*, E. P. Chassignet and J. Verron, Eds., NATO Science Series, Vol. 16, Springer, 1–44.

Menary, M. B., D. L. R. Hodson, J. I. Robson, R. T. Sutton, R. A. Wood, and J. A. Hunt, 2015: Exploring the impact of CMIP5 model biases on the simulation of North Atlantic decadal variability. *Geophys. Res. Lett.*, **42**, 5926–5934, https://doi.org/10.1002/2015GL064360.

Monterey, G. I., and L. M. deWitt, 2000: Seasonal variability of global mixed layer depth from WOD98 temperature and salinity profiles. NOAA Tech. Memo NMFS-SWFSC-296, 61 pp., https://repository.library.noaa.gov/view/noaa/3160.

Ortega, P., J. Robson, R. T. Sutton, and M. B. Andrews, 2017: Mechanisms of decadal variability in the Labrador Sea and the wider North Atlantic in a high-resolution climate model. *Climate Dyn.*, **49**, 2625–2647, https://doi.org/10.1007/s00382-016-3467-y.

Oschlies, A., 2002: Improved representation of upper-ocean dynamics and mixed layer depths in a model of the North Atlantic on switching from eddy-permitting to eddy-resolving grid resolution. *J. Phys. Oceanogr.*, **32**, 2277–2298, https://doi.org/10.1175/1520-0485(2002)032<2277:IROUOD>2.0.CO;2.

Rattan, S., P. G. Myers, A.-M. Treguier, S. Theetten, A. Biastoch, and C. Böning, 2010: Towards an understanding of Labrador Sea salinity drift in eddy-permitting simulations. *Ocean Modell.*, **35**, 77–88, https://doi.org/10.1016/j.ocemod.2010.06.007.

Redi, M. H., 1982: Oceanic isopycnal mixing by coordinate rotation. *J. Phys. Oceanogr.*, **12**, 1154–1158, https://doi.org/10.1175/1520-0485(1982)012<1154:OIMBCR>2.0.CO;2.

Renault, L., M. J. Molemaker, J. Gula, S. Masson, and J. C. McWilliams, 2016: Control and stabilization of the Gulf Stream by oceanic current interaction with the atmosphere. *J. Phys. Oceanogr.*, **46**, 3439–3453, https://doi.org/10.1175/JPO-D-16-0115.1.

Rhein, M., and Coauthors, 2011: Deep water formation, the subpolar gyre, and the meridional overturning circulation in the subpolar North Atlantic. *Deep-Sea Res. II*, **58**, 1819–1832, https://doi.org/10.1016/j.dsr2.2010.10.061.

Robinson, I. S., 2010: *Discovering the Ocean from Space: The unique Applications of Satellite Oceanography*. Springer, 638 pp.

Sarafanov, A., and Coauthors, 2012: Mean full-depth summer circulation and transports at the northern periphery of the Atlantic Ocean in the 2000s. *J. Geophys. Res.*, **117**, C01014, https://doi.org/10.1029/2011JC007572.

Scaife, A. A., and Coauthors, 2014: Skillful long-range prediction of European and North American winters. *Geophys. Res. Lett.*, **41**, 2514–2519, https://doi.org/10.1002/2014GL059637.

Scholz, P., G. Lohmann, Q. Wang, and S. Danilov, 2013: Evaluation of a Finite-Element Sea-Ice Ocean Model (FESOM) set-up to study the interannual to decadal variability in the deep-water formation rates. *Ocean Dyn.*, **63**, 347–370, https://doi.org/10.1007/s10236-012-0590-0.

——, D. Kieke, G. Lohmann, M. Ionita, and M. Rhein, 2014: Evaluation of Labrador Sea Water formation in a global Finite-Element Sea-Ice Ocean Model setup, based on a comparison with observational data. *J. Geophys. Res. Oceans*, **119**, 1644–1667, https://doi.org/10.1002/2013JC009232.

Schourup-Kristensen, V., D. Sidorenko, D. A. Wolf-Gladrow, and C. Völker, 2014: A skill assessment of the biogeochemical model REcoM2 coupled to the Finite Element Sea Ice-Ocean Model (FESOM 1.3). *Geosci. Model Dev.*, **7**, 2769–2802, https://doi.org/10.5194/gmd-7-2769-2014.

Sein, D. V., and Coauthors, 2017: Ocean modeling on a mesh with resolution following the local Rossby radius. *J. Adv. Model. Earth Syst.*, **9**, 2601–2614, https://doi.org/10.1002/2017MS001099.

Sidorenko, D., Q. Wang, S. Danilov, and J. Schröter, 2011: FESOM under coordinated ocean-ice reference experiment forcing. *Ocean Dyn.*, **61**, 881–890, https://doi.org/10.1007/s10236-011-0406-7.

Smagorinsky, J., 1963: General circulation experiments with the primitive equations. *Mon. Wea. Rev.*, **91**, 99–164, https://doi.org/10.1175/1520-0493(1963)091<0099:GCEWTP>2.3.CO;2.

Smeed, D., G. McCarthy, D. Rayner, B. Moat, W. Johns, M. Baringer, and C. Meinen, 2017: Atlantic meridional overturning circulation observed by the RAPID-MOCHA-WBTS (RAPID-Meridional Overturning Circulation and Heatflux Array-Western Boundary Time Series) array at 26N from 2004 to 2017. British Oceanographic Data Centre, Natural Environment Research Council, https://doi.org/10.5285/5acfd143-1104-7b58-e053-6c86abc0d94b.

Steele, M., R. Morley, and W. Ermold, 2001: PHC: A global ocean hydrography with a high-quality Arctic Ocean. *J. Climate*, **14**, 2079–2087, https://doi.org/10.1175/1520-0442(2001)014<2079:PAGOHW>2.0.CO;2.

Stewart, K., A. Hogg, S. Griffies, A. Heerdegen, M. Ward, P. Spence, and M. England, 2017: Vertical resolution of baroclinic modes in global ocean models. *Ocean Modell.*, **113**, 50–65, https://doi.org/10.1016/j.ocemod.2017.03.012.

Talandier, C., and Coauthors, 2014: Improvements of simulated western North Atlantic current system and impacts on the AMOC. *Ocean Modell.*, **76**, 1–19, https://doi.org/10.1016/j.ocemod.2013.12.007.

Timmermann, R., S. Danilov, J. Schröter, C. Böning, D. Sidorenko, and K. Rollenhagen, 2009: Ocean circulation and sea ice distribution in a finite element global sea ice-ocean model. *Ocean Modell.*, **27**, 114–129, https://doi.org/10.1016/j.ocemod.2008.10.009.

Treguier, A. M., S. Theetten, E. P. Chassignet, T. Penduff, R. Smith, L. Talley, J. O. Beismann, and C. Böning, 2005: The North Atlantic subpolar gyre in four high-resolution models. *J. Phys. Oceanogr.*, **35**, 757–774, https://doi.org/10.1175/JPO2720.1.

Vallis, G. K., 2017: *Atmospheric and Oceanic Fluid Dynamics: Fundamentals and Large-Scale Circulation*. 2nd ed. Cambridge University Press, 745 pp.

Wang, C., L. Zhang, S.-K. Lee, L. Wu, and C. R. Mechoso, 2014: A global perspective on CMIP5 climate model biases. *Nat. Climate Change*, **4**, 201–205, https://doi.org/10.1038/nclimate2118.

Wang, Q., S. Danilov, and J. Schröter, 2008: Finite element ocean circulation model based on triangular prismatic elements, with application in studying the effect of topography representation. *J. Geophys. Res.*, **113**, C05015, https://doi.org/10.1029/2007JC004482.

——, ——, H. H. Hellmer, and J. Schröter, 2010: Overflow dynamics and bottom water formation in the western Ross Sea: Influence of tides. *J. Geophys. Res.*, **115**, C10054, https://doi.org/10.1029/2010JC006189.

——, ——, D. Sidorenko, R. Timmermann, C. Wekerle, X. Wang, T. Jung, and J. Schröter, 2014: The Finite Element Sea Ice-Ocean Model (FESOM) v.1.4: Formulation of an ocean general circulation model. *Geosci. Model Dev.*, **7**, 663–693, https://doi.org/10.5194/gmd-7-663-2014.

Wang, X., Q. Wang, D. Sidorenko, S. Danilov, J. Schröter, and T. Jung, 2012: Long-term ocean simulations in FESOM: Evaluation and application in studying the impact of Greenland Ice Sheet melting. *Ocean Dyn.*, **62**, 1471–1486, https://doi.org/10.1007/s10236-012-0572-2.

Weese, S. R., and F. O. Bryan, 2006: Climate impacts of systematic errors in the simulation of the path of the North Atlantic Current. *Geophys. Res. Lett.*, **33**, L19708, https://doi.org/10.1029/2006GL027669.

Wekerle, C., W. Wang, S. Danilov, T. Jung, and J. Schröter, 2013: The Canadian Arctic Archipelago throughflow in a multi-resolution global model: Model assessment and the driving mechanism of interannual variability. *J. Geophys. Res. Oceans*, **118**, 4525–4541, https://doi.org/10.1002/jgrc.20330.

Willis, J. K., 2010: Can in situ floats and satellite altimeters detect long-term changes in Atlantic Ocean overturning? *Geophys. Res. Lett.*, **37**, L06602, https://doi.org/10.1029/2010GL042372.

Wunsch, C., 1997: The vertical partition of oceanic horizontal kinetic energy. *J. Phys. Oceanogr.*, **27**, 1770–1794, https://doi.org/10.1175/1520-0485(1997)027<1770:TVPOOH>2.0.CO;2.

Xu, X., H. E. Hurlburt, W. J. Schmitz, R. Zantopp, J. Fischer, and P. J. Hogan, 2013: On the currents and transports connected with the Atlantic meridional overturning circulation in the subpolar North Atlantic. *J. Geophys. Res. Oceans*, **118**, 502–516, https://doi.org/10.1002/jgrc.20065.

Yashayaev, I., and J. W. Loder, 2017: Further intensification of deep convection in the Labrador Sea in 2016. *Geophys. Res. Lett.*, **44**, 1429–1438, https://doi.org/10.1002/2016GL071668.

Zhang, R., T. L. Delworth, A. Rosati, W. G. Anderson, K. W. Dixon, H. Lee, and F. Zeng, 2011: Sensitivity of the North Atlantic Ocean Circulation to an abrupt change in the Nordic Sea overflow in a high resolution global coupled climate model. *J. Geophys. Res.*, **116**, C12024, https://doi.org/10.1029/2011JC007240.

Zweng, M. M., and Coauthors, 2013: *Salinity*. Vol. 2, *World Ocean Atlas 2013*, NOAA Atlas NESDIS 74, 39 pp., https://www.nodc.noaa.gov/OC5/woa13/pubwoa13.html.